Science
AAAS

Supplementary Materials for

More resilient polyester membranes for high-performance reverse osmosis desalination

Yujian Yao *et al*.

Corresponding authors: Xianze Wang, wangxz940@nenu.edu.cn; Xuan Zhang, xuanzhang@njust.edu.cn; Menachem Elimelech, menachem.elimelech@yale.edu

Science **384**, 333 (2024)
DOI: 10.1126/science.adk0632

The PDF file includes:

MATERIALS AND METHODS

Materials and Chemicals.

Hydrochloric acid (HCl) and sodium hypochlorite aqueous solution (NaOCl, 10% available chlorine) were purchased from Sinopharm Chemical Reagent Co. Ltd. (Shanghai, China). Trimesoyl chloride (TMC, >99%), 3,5-dihydroxybenzoic acid (DHBA, >99%), isophthaloyl chloride (IPC, >99%), piperazine (PIP, >99%), trimethylamine (TEA, >99%), camphorsulfonic acid (CSA, >99%), silver nitrate (>99%), indium nitrate (>99%), sodium hydroxide (NaOH, >99%), nitric acid (HNO_3, >99%), sodium dodecyl sulfate (SDS), ethylene glycol, erythritol, and xylose were purchased from *J&K* Chemical Reagent Co. Ltd. (Beijing, China). Bromine, *N*,*N*-dimethylformamide (DMF), chloroform, ethanol, ethyl acetate, acetone, and *n*-hexane were purchased from Nanjing Chemical Reagent Co. Ltd. (Nanjing, China). Acetic acid (CH_3COOH, >99.8%) was purchased from Titan Scientific Co. Ltd. (Shanghai, China). Dimethylamine (40 wt% solution in water) was purchased from Energy Chemical Co., Ltd. (Anhui, China). Raney nickel (50 μm) was purchased from Macklin Biochemical Co., Ltd. (Shanghai, China). Poly(ether sulfone) (PES) ultrafiltration membrane substrates [5 kDa molecular weight cut-off (MWCO); 55.5±2.7 L m^{-2} h^{-1} water flux at 0.1 MPa] were purchased from RisingSun Membrane Technology Co. Ltd. (Beijing, China). Commercial BW30 and SW30 reverse osmosis (RO) membranes were supplied by DuPont Company (USA). All reagents were used as received. Deionized (DI) water (resistance >18 MΩ-cm) was used throughout this study.

Synthesis of DHMBA (3,5-dihydroxy-4-methylbenzoic acid).

A solution of bromine (8.530 mL/166.6 mmol, in 35.00 mL of $CHCl_3$) was added to a solution of 3,5-dihydroxybenzoic acid (12.32 g, 80.00 mmol) in $CHCl_3$ (135.0 mL) at 22 °C over 15 min through a constant pressure dropping funnel. After that, the reaction solution was continuously stirred for 5 hours. During the reaction, the funnel was equipped with an outlet for dissolving the gas (HBr) into the NaOH solution (5 wt%). The white precipitates (2,6-dibromo-3,5-dihydroxybenzoic acid, ***M1***) were filtered, washed with $CHCl_3$ and cold H_2O, and dried under vacuum at 60 °C overnight (24.29 g, yield of 97%).

FTIR (KBr, υ, cm^{-1}): 1672 (C=O), 1580 (C=C), 1212 (C–O), and 1057 (C–Br); ^{1}H NMR (D_2O, δ, ppm): 6.52 (s, Ar–H); ^{13}C NMR (D_2O, δ, ppm): 170.91, 153.29, 139.41, 104.32, and 96.41; LC-MSMS: 311.1 [M-H].

Ethanol (30.00 mL) and acetic acid (55.00 mL) were added dropwise to a solution initially mixed with 37% aqueous formaldehyde (4.678 g, 156.0 mmol) and 40% aqueous dimethylamine (7.032 g, 156.0 mmol) at room temperature. After that, ***M1*** (24.29 g, 78.00 mmol) was added to the mixture and the solution was kept stirring at room temperature for another 24 hours. Complete precipitation of the product was achieved by cooling the reaction mixture to 0 °C for 1 hour. The product (2,6-dibromo-4-((dimethylamino)methyl)-3,5-dihydroxybenzoic acid, ***M2***) was filtered, washed with cold acetone, and dried under vacuum at 60 °C to afford a white powder (27.60 g, yield of 96%).

FTIR (KBr, υ, cm^{-1}): 1710 (C=O), 1605 (C=C), 1255 (C–O), 1204 (C–N), and 1088 (C–Br); ^{1}H NMR (DMSO-d_6, δ, ppm): 2.54 (s, –N–CH_2–) and 1.94 (s, –CH_3); ^{13}C NMR (DMSO-d_6, δ, ppm): 172.47, 154.37, 141.56, 110.36, 98.93, 52.27, and 43.20; LC-MSMS: 368.0 [M-H].

A three-necked flask equipped with nitrogen inlet/outlet and a magnetic stirrer was added ***M2*** (23.45 g, 63.55 mmol) and 160 mL of NaOH (aq., 3 M). Maintaining the solution temperature at 25–30 °C, Raney nickel (21.87 g) was portion-wise added into the solution over a period of 2 hours. After that, the resulting mixture was stirred at room temperature for another 12 hours before the solution was filtered through a pad of celite. The crude product was washed

with DI water and the filtrate was further acidified in an HCl solution (pH ~1.0). The resulting mixture was extracted with ethyl acetate three times, and the combined organic phases were sequentially washed with DI water, brine, and anhydrous Na_2SO_4, and then concentrated with a rotary evaporator. The residue was dried under vacuum at 60 ^oC overnight to afford a white powder (DHMBA, 10.35 g, yield of 97%).

FTIR (KBr, υ, cm^{-1}): 2898 (C–H), 1695 (C=O), 1601 (C=C), and 1226 (C–O); ^1H NMR (D_2O, δ, ppm): 6.94 (s, Ar–H), and 2.02 (s, $–CH_3$); ^{13}C NMR (D_2O, δ, ppm): 170.17, 154.70, 127.89, 118.11, 108.44, and 8.21; LC-MSMS: 166.8 [M-H].

Computational Methods.

Density functional theory (DFT) calculations were performed using the $DMol^3$ module (*22*,*23*) in Materials Studio. The exchange–correlation energy was described by the Generalized Gradient Approximation (GGA) based on the Becke−Lee−Yang−Parr (BLYP) functional (*24*,*25*). For the calculations, we used the double-numerical plus polarization (DNP) basis set with all electrons considered. All the calculations were performed using the spin-polarized Kohn-Sham formalism with a real-space cutoff of 6.0 Å. In order to consider the liquid-phase environment, the Conductor-like Screening Model (COSMO) (*26*,*27*) was employed with the dielectric constant (ε) of 78.4 a.u. for water. Additionally, potential energy scans were carried out by *ab initio* program package Gaussian 09 (*28*) at the B3LYP theoretical level using 6-31G(d,p) basis functions.

The atomic charge distribution of the molecules was considered using the Mulliken population. To systematically analyze the frontier molecular orbital characteristics, the highest occupied molecular orbital (HOMO) and the lowest unoccupied molecular orbital (LUMO) were calculated. The Fukui functions (*29*) were also investigated here to show the reactivity of a molecule with respect to electrophilic or nucleophilic attack. Aiming to qualitatively display the electrophilic reactivity of the molecular regions, the condensed Fukui functions (f_k^-) were calculated for the electrophilic attack reaction based on

$$f_k^- = q_k - q_k^{cation} \tag{S1}$$

where q_k and q_k^{cation} are the atomic-centered charges in a neutral and a cationic system, respectively, which are both computed from the Mulliken population analysis.

Membrane Preparation Procedure.

Fabrication of DHMBA membrane: In brief, the PES substrate was immersed in an aqueous solution containing 4.0 wt% DHMBA and 1.44 wt% NaOH for at least five minutes. After that, the membrane sheet was taken out from the solution and the residual droplets on the surface were removed using a rubber roller. The membrane was then fixed to a frame (active area of 10 cm × 10 cm) with the skin layer exposed outward, and a chloroform/*n*-hexane (1/4, v/v) solution containing 0.2 wt% TMC was poured onto the surface. The TMC solution was allowed to contact the substrate for two minutes. Afterward, the organic solution was drained, and the membrane surface was rinsed with fresh *n*-hexane to remove any unreacted TMC molecules. Immediately after the *n*-hexane solution was drained, 100 mL of fresh *n*-hexane solution containing 2.0 wt% IPC was poured onto the membrane surface for the end-capping of residual −OH groups (*30*). After static immersion for five minutes, the solution was drained, and the surface was rinsed again with fresh *n*-hexane (100 mL). Finally, the thin-film composite (TFC) membrane (named DHMBA) was air-dried and stored in DI water until use.

Fabrication of DHMBA-EA/HEX and DHMBA-HEX membranes: In brief, these two types of membranes were fabricated by the similar IP method mentioned above. Specifically, an ethyl acetate/*n*-hexane (1/3, v/v) solution containing 0.2 wt% TMC was used for the fabrication of the DHMBA-EA/HEX membrane, whereas a sole *n*-hexane solution containing 0.2 wt% TMC was used for the fabrication of the DHMBA-HEX membrane, respectively. Afterward, the same end-capping procedure mentioned above was conducted on both membranes. Here, EA and HEX denote the ethyl acetate and *n*-hexane used for the membrane fabrication.

Fabrication of PIP-DHBA-DHBA membrane: The PIP-DHBA-DHBA membrane was fabricated by a layer-by-layer IP technique, according to our previous report (*9*). In brief, the PES substrate was immersed in an aqueous solution containing 0.35 wt% PIP, 2.0 wt% TEA, and 1.0 wt% CSA for two minutes. After that, the membrane sheet was taken out from the solution and the residual water droplets on the surface were removed using a rubber roller. The amine-saturated membrane was then fixed to a frame with the skin layer exposed outward, and an *n*-hexane solution containing 0.15 wt% TMC was poured onto the surface, allowing contact for 60 seconds. Afterward, the organic solution was drained, and the membrane surface was rinsed with fresh *n*-hexane to remove any unreacted molecules. After complete evaporation of residual *n*-hexane on the membrane surface, another aqueous solution containing 2.0 wt% DHBA and 1.56 wt% NaOH was poured onto the surface for reacting with the residual –COCl groups (five minutes). The membrane sheet was taken out from the solution, and the *n*-hexane solution containing 0.15 wt% TMC was poured onto the membrane surface and left for another two minutes. Next, another aqueous solution containing 2.0 wt% DHBA and 1.56 wt% NaOH was poured onto the surface for reacting with the residual –COCl groups (two minutes). The membrane sheet was then taken out from the solution, and the *n*-hexane solution containing 0.15 wt% TMC was poured onto the membrane surface. After two minutes, the organic solution was drained, and the membrane surface was rinsed with fresh *n*-hexane to remove any unreacted molecules. Finally, end-capping of residual –OH groups was conducted with the same procedures described above. The prepared TFC membrane (named PIP-DHBA-DHBA) was air-dried and stored in DI water until it was tested.

Desalination Performance Tests.

Membranes were tested for their separation performance using a custom-made crossflow equipment with an effective membrane area of 15.0 cm^2 (3 cm × 5 cm). For desalination of low-salinity waters, pure water was initially used as the feed solution at a crossflow rate of 40.0 cm s^{-1} at 25±1 °C to ensure a stable water permeation at a pressure of 20.0 bar for at least one hour. After that, an NaCl solution with a concentration of 2,000 mg L^{-1} (pH 6.9±0.1, 25°C) was used as the feed solution. Membrane performance tests were then performed at a constant pressure of 15.5 bar. The water flux J_w (L m^{-2} h^{-1}) of the membrane was calculated using the following equation:

$$J_w = \frac{V}{A_m \Delta t} \tag{S2}$$

where V is the volume of the permeated water, A_m is the effective membrane area, and Δt is the permeation time. The water permeance or water permeability coefficient, A, was calculated from

$$A = \frac{J_w}{\Delta P} \tag{S3}$$

where ΔP is the applied pressure.

The salt rejection R was calculated using

$$R = \left(1 - \frac{C_p}{C_f}\right) \times 100\% \tag{S4}$$

where C_p (mg L^{-1}) is the mass concentration of the permeate and C_f (mg L^{-1}) is the mass concentration of the feed. The concentrations of the NaCl solution in both the feed and the permeate were measured using a DDS-307 Conductivity Meter (Baoshishan, Shanghai, China). The salt permeability coefficient, B, was then determined from (*31*)

$$B = \frac{J_s}{\Delta C_f \exp\left(\frac{J_w}{k_f}\right)} \tag{S5}$$

where J_s is the salt flux, ΔC_f is the salt concentration difference across the membrane, and k_f is the solute mass transfer coefficient. Specifically, the k_f was calculated to be 98.6 L m^{-2} h^{-1} for NaCl as determined from the film theory for cell geometry (*31*).

All membrane sheets were prepared in duplicate. At least two measurements were taken for each sample and then reported as the average.

For testing seawater desalination performance, a simulated seawater sample was used as a feed solution (table S4). The pH of the feed was 7.7±0.1 and the operation pressure was fixed at 55 bar throughout the test. The concentration of the cations was measured by atomic absorption spectroscopy (AAS) (Z-5000, Hitachi, Japan), and the concentration of the anions was measured by ion chromatography (IC) (ICS-2100, Thermo Fisher Scientific, USA).

For the gypsum scaling (single factor) experiments, a 5 L mixed solution containing 1 g L^{-1} (7.04 mM) Na_2SO_4 and 1 g L^{-1} (9.01 mM) $CaCl_2$ was prepared and used as the feed, corresponding to a saturation index (SI) value of 0.51. For the gypsum scaling (multifactor) experiments, a 5 L simulated seawater (table S4) was directly used as feed, corresponding to an SI value of 0.52. Note that the operating pressures were adjusted separately for each operation to ensure the same initial water flux of both DHMBA and SW30 membranes. The permeate was recycled back to the feed tank over the entire operation (24 hours).

For the fouling tests, a 5 L simulated seawater (table S4) with 20 mg L^{-1} humic acid (HA) or 20 mg L^{-1} sodium alginate (SA) was prepared. The pH of the feed was 7.7±0.1 and the operating pressures were adjusted separately for each operation to ensure the same initial water flux across all tests. Prior to each scaling and/or fouling experiment, a new piece of membrane coupon was equilibrated with DI water at 55 bar overnight until a constant permeate flux was achieved. The permeate was recycled back to the feed tank over the entire operation (24 hours).

Chlorine resistance tests were performed using a static approach. Briefly, individual membrane samples were initially immersed in an NaOCl solution under continuous stirring, with the pH adjusted by HCl (aq., 1.0 M) to 0, 7.0, or 9.0. At specified times, membrane samples were taken out from the solution, rinsed thoroughly with DI water, and placed into RO cells. The water flux and NaCl rejection (obtained via solution conductivity) of the membranes

were recorded to monitor the possible degradation of the membrane. The total free Cl exposure of the RO membrane was calculated as CT_{FC} (ppm·h) $=\int C_{FC} dt$, where C_{FC} refers to the total concentration of the free chlorine solution.

Desalination Tests with Practical Seawater.

For practical seawater desalination experiments, 5 L of real seawater (table S4, Qingdao City, China, 120.0358°E, 35.8139°N) was sterilized with 5 mg L^{-1} chlorine (NaOCl) and pre-filtered with 40 μm filter paper. The filtrate solution (pH 8.2±0.1) was then directly used as the feed for the RO test. The permeate was recycled back to the feed tank over the entire operation (15 days).

QCMD Analysis.

The real-time crystal formation of $CaSO_4 \cdot 2H_2O$ was characterized using a quartz crystal microbalance with dissipation (QCMD) (Q-Sense E4 analyzer, Biolin Scientific, Sweden). A mass sensitivity and a dissipation sensitivity of 1.8 ng cm^{-2} and 0.1×10^{-6} in liquid were preset to the instrument, respectively. Prior to testing, the Au sensors (Q-Sense) were cleaned in 2% SDS solution, pure water, dried with N_2, and cleaned in a UV/Ozone ProCleaner (Bioforce) for 15 minutes.

To perform the QCMD experiments, free-standing DHMBA membrane samples were prepared by the IP method. In brief, an aqueous phase containing DHMBA monomers was placed in a beaker and then covered with a chloroform/*n*-hexane solution containing TMC (same as the procedure mentioned above). For the SW30 membrane, its polyamide layer was taken by floating the membrane on DMF solvent, resulting in the delamination of the active layer and the substrate. Here, both membrane samples were carefully taken out from the solution, rinsed with water, and transferred to the QCMD sensor. The coated sensors were then mounted in two parallel QCMD cells, and the experiments used the same testing condition as in the scaling experiments (i.e., solutions SI of 0.51 or 0.52) at 25±1 °C. The frequency and dissipation data were continuously monitored for each coated sensor over the entire test.

The increase of adsorbed or precipitated mass (Δm, ng cm^{-2}) on the sensors was calculated from the frequency change using the Sauerbrey equation (*32*):

$$\Delta m = -C \frac{\Delta f}{n} \tag{S6}$$

where C is the mass sensitivity constant (which is related to the properties of the quartz sensors and equals 17.7 ng cm^{-2} Hz^{-1} in this study), Δf is the frequency change (Hz), and n is the harmonic number (n = 5 in this study).

Calculation of the Saturation Index (SI).

In the scaling experiments, the degree of supersaturation with respect to gypsum was quantified in terms of the gypsum saturation index (SI), defined as (*33*)

$$\mathrm{SI} = \frac{\gamma_{Ca^{2+}} \cdot [Ca^{2+}] \cdot \gamma_{SO_4^{2-}} \cdot [SO_4^{2-}] \cdot a_w^2}{K_{sp}} \tag{S7}$$

where K_{sp} is the solubility product constant of gypsum in water (K_{sp} = 2.623 × 10^{-5} at 20 ºC); $\gamma_{Ca^{2+}}$, $\gamma_{SO_4^{2-}}$, and [Ca^{2+}], [SO_4^{2-}] are the activity coefficients and the concentrations (M) of Ca^{2+} and SO_4^{2-}, respectively; and a_w is the activity of water ($a_w = 1$). The activity coefficients of ion species ($\gamma_{Ca^{2+}}$ and $\gamma_{SO_4^{2-}}$) at different ionic strength (I) conditions can be

estimated by Davies' approximation (i.e., $I \leq 0.5$ M) and Truesdell-Jones' approximation (i.e., 0.5 M < I < 1 M), without taking ion pair formation into account (*34*):

Davies
$$\log\gamma_i = -Az_i^2\left(\frac{\sqrt{I}}{1+\sqrt{I}} - 0.3I\right) \quad \text{(S8)}$$

Truesdell-Jones
$$\log\gamma_i = -Az_i^2\left(\frac{\sqrt{I}}{1+Ba_i^0\sqrt{I}}\right) + b_i I \quad \text{(S9)}$$

$$A = 1.82 \times 10^6(\varepsilon T)^{-3/2} \quad \text{(S10a)}$$
$$B = 50.3 \times (\varepsilon T)^{-3/2} \quad \text{(S10b)}$$
$$I = \frac{1}{2}\sum z_i^2 c_i \quad \text{(S10c)}$$

where z_i is the ion charge, c_i is the ion concentration of specific ions (M), ε is the dielectric constant of water (ε = 78.4), and T is the absolute temperature (K). The a_i^0 parameter for Ca^{2+} and SO_4^{2-} in the solution is 5, and the b_i parameter values for Ca^{2+} and SO_4^{2-} in solution are 0.165 and -0.040, respectively (*35*). When Ca^{2+} and SO_4^{2-} are supersaturated in solution, they do not precipitate immediately and need an induction time for precipitation reaction, as hypothesized by the classic nucleation theory. During the crystal growth stage, clusters of $CaSO_4{\cdot}2H_2O$ take time to form microcrystals via the attachment of solute species (*i.e.*, Ca^{2+} and SO_4^{2-}) or aggregation of clusters/nuclei and fully developed nanosized crystals.

Adhesion Force Measurements.

Interaction forces between the RO membranes and the model organic foulants (alginate and humic acid) were evaluated using atomic force microscopy (AFM). The force measurements were performed with a carboxylate-modified polystyrene particle (diameter of 4.5 μm) probe functionalized on a silicon nitride cantilever (Novascan Technologies, Inc., USA). The carboxylate-modified polystyrene particle simulates organic foulants due to its carboxyl functional groups, which are also abundant in alginate and humic acid (*36*). The AFM measurements were conducted in a fluid cell containing 1 mM $NaHCO_3$ and 0.5 mM $CaCl_2$ solution (pH 8.0±0.1). Cantilever deflection versus separation distance data were collected in AFM contact mode for the probe particle approaching and retracting from the membrane surfaces. A model fused silica wafer was used to calibrate the cantilever deflection sensitivity and spring constant. At least 50 measurements were collected on five random locations of each membrane sample to minimize the inherent variability in the force data, which is mainly attributed to the heterogeneity of the membrane surface. Only the retracting force data, representing the maximum adhesion force between the membrane surface and the particle probe, were analyzed with Nanoscope Analysis Software (Version 1.90, Bruker Corporation).

Atom Probe Tomography (APT) Measurements.

Needle-shaped specimens were prepared with a Zeiss Auriga CrossBeam focused ion beam (FIB)/scanning electron microscope (SEM) system, under an accelerating voltage of 30 kV and a beam current of 50 pA in the final milling step. First, gold sputtering was performed on the surfaces of the two membranes to obtain clear images in SEM (gold sputtering current: 20 mA, duration: 25 s). Then, a protective layer of Pt was deposited under focused ion beam (FIB) to prevent damage to the sample surface caused by Ga ion irradiation (Pt deposition length: 15 micrometers, thickness: 0.5 micrometers, focused ion-beam current: 20 pA). After depositing

Pt, ion milling on each side of the Pt-protected region was performed to produce a wedge-shaped bar from the sample surface. First, a square trench normal to the sample surface was dug on one end of the stripe to facilitate the insertion and gripping of the nanomanipulator. Then, the other two trenches at 30° to the surface normal were dug on each long side of the stripe. When the bottom of the stripe was separated from the substrate, the nanomanipulator was inserted from the side and brought into contact with the picked sample stripe. Pt (0.5-micrometer thickness) was deposited at the contact between the nanomanipulator and the picked sample to create suitable welding. After the deposition, the last short side of the picked sample was cut using a Ga ion beam (cutting current: 1 nA). After a successful separation secured by the cutting, the nanomanipulator was used to lift the wedge-shaped bar out from the bulk sample. The wedge-shaped bar sample on the nanomanipulator was placed on a silicon array micron-tip with Pt deposition and followed with Ga beam cutting to leave a section of the wedge-shape on the top of the Si array tip. Finally, annular milling was performed to produce a sharp tip using the focused ion beam (currents used: 600 mA, 240 pA, 120 pA, 50 pA). APT data acquisitions were performed on a LEAP 4000X Si (CAMECA Scientific Instruments, France) under a pulsing UV laser with a wavelength of 355 nm, at a specimen temperature of 40 K, a pulse frequency of 200 kHz, a pulse energy of 90 pJ, and a targeted evaporation rate of 0.2%. APT data reconstruction and analysis were done using the shank angle algorithm with AP Suite 6.1 software.

Time-of-Flight Secondary Ion Mass Spectrometry (ToF-SIMS) Analysis.

ToF-SIMS was applied to characterize the SW30 and DHMBA membranes on a ToF-SIMS5 instrument (ION-ToF-GmbH, Germany). A pulsed 30 KeV Bi^{3+} ion beam was set with an analysis area of 150 μm × 150 μm. Then the 30 KeV Bi^{3+} ion beam with the incident angle of 45° was applied to sputter the membranes.

Quantifying Membrane Carboxyl Group Density.

The carboxyl group density of both RO membranes was measured using the silver ion binding method (*37*). In brief, the membrane coupons (2 cm × 2 cm) were immersed twice, each for 10 min, in 10 mL of 40 μM silver nitrate solution at the desired pH conditions (pH 3.5, 5, 7, 9, 10, and 10.5, adjusted by NaOH and HNO_3 solutions). After the binding step, membranes were immersed four times, each for seven minutes, in 10 mL of 1 μM silver nitrate solution at the same pH condition to rinse off unbound silver. The membranes were touched lightly against a filter paper for each step to minimize solution carryover. Afterward, membranes were immersed in 5 mL of 1% HNO_3 for 30 minutes to protonate the carboxyl groups and elute the bound silver ions. After the physical removal of the silver-free membranes, the extracted solutions were subjected to ICP-MS (Agilent 7900, USA) analysis. HNO_3 solutions (1%) with silver concentrations ranging from 0 to 200 μg L^{-1} were used to calibrate the system. Indium nitrate (40 μg L^{-1}) was used as an internal standard for ICP-MS.

To convert the silver concentration to areal and volumetric carboxyl group density, it was assumed that silver ions could bind with all ionized carboxyl groups within the membrane matrixes and each eluted silver ion corresponded to one ionized carboxyl group (i.e., 1:1 binding) (*37*). The areal concentration of ionized carboxyl was determined using:

$$[\mathrm{R-COO^-}]_{A_m} = \frac{C_{Ag+} V_{Ag+} N_A}{A_m} \tag{S11}$$

where $[\mathrm{R-COO^-}]_{A_m}$ is the ionized carboxyl group areal density (number of groups per unit area, sites nm^{-2}), A_m is the projected surface area of the membranes (i.e., 4 cm^2), C_{Ag+} is the silver molar concentration measured by ICP-MS, V_{Ag+} is the elution volume, and N_A is

Avogadro's number. The projected surface area is defined as the single-sided surface area of the membrane sample, neglecting surface roughness.

We also divided the areal $\mathrm{R-COO^-}$ density by the dry film thickness (δ_d, obtained by TEM), to calculate the volumetric $\mathrm{R-COO^-}$ density, $[\mathrm{R-COO^-}]_{V_m} = [\mathrm{R-COO^-}]_{A_m} / \delta_\mathrm{d}$ (number of groups per nm^3). The concentration of $\mathrm{R-COO^-}$ as a function of pH is fitted by the following acid−base equilibrium expression (*38*),

$$[R-COO^-] = C_{\mathrm{T,R-COOH}} \sum_{i=1}^{n} \left(w_i \frac{10^{-pK_{\mathrm{a},i}}}{10^{-pH} + 10^{-pK_{\mathrm{a},i}}} \right) \tag{S12}$$

where $C_{\mathrm{T,R-COOH}}$ is the total concentration of carboxylic groups ($\mathrm{R-COOH}$ and $\mathrm{R-COO^-}$), $p\mathrm{K_{a,i}}$ is the ith logarithmic dissociation constant of carboxylic group, and w_i is the fraction of carboxylic group with logarithmic dissociation constant $p\mathrm{K_{a,}}_i$ (i.e., $w_1 + w_2 + \cdots + w_i = 1$). As reported previously, two dissociation constants (i.e., n = 2) were used to fit the ionization of the carboxyl group at different pH (*38*).

Estimating RO Membrane Pore Size.

The effective pore sizes of the membranes were estimated by fitting the rejection of various neutral solutes (ethylene glycol, erythritol, and xylose) to the hydrodynamic pore flow model (*38*). A fixed concentration of 50 mg L^{-1} (as total organic carbon, TOC) was prepared for each solute in the filtration tests. Membrane coupons (area of 15.0 cm^2) were mounted into a custom-made crossflow filtration system and were equilibrated with DI water at 31.7 bar for over 8 hours before the solute rejection test. Permeate was collected at pressures of 27.6, 20.7, 13.8, and 6.9 bar with the crossflow rate maintained at 21.4 cm s^{-1} for the SW30 and DHMBA membranes. For each operation condition, the system was stabilized for 1 hour before sample collection. Membrane permeate flux (J_w, μm s^{-1}) was recorded at each pressure, while the solute concentration in the feed solution and permeate was analyzed by the TOC instrument (multi N/C 2100, Germany) to obtain the observed solute rejection (R_O). According to the film theory for concentration polarization, the real rejection of the solutes (R_r) can be calculated via the following equation (*39*):

$$\ln\frac{1-R_\mathrm{r}}{R_\mathrm{r}} = \ln\frac{1-R_\mathrm{o}}{R_\mathrm{o}} - \frac{J_\mathrm{w}}{k_\mathrm{f}} \tag{S13}$$

where k_f is the mass transfer coefficient.

The steps to estimate the effective pore size based on the real rejection data of the neutral solutes are detailed in ref (*39*).

Characterization.

The chemical structures of all monomers were characterized using Fourier transform infrared (FTIR) spectroscopy (Nicolet IS-10, Thermo Scientific, USA) in the frequency range 500–4000 cm^{-1} with 32 scans per spectrum, ^{1}H (500 MHz) and ^{13}C (75 MHz) nuclear magnetic resonance (NMR) spectra on a Bruker AVANCE III spectrometer using D_2O or DMSO-d_6 as the solvent, and ultrahigh performance liquid chromatography and mass spectrometry (UPLC-MS/MS) on a QTRAP® 4500 spectrometer (AB SCIEX, USA). UV-Vis spectrophotometer (UV-2700, Shimadzu, Japan) was used to in situ monitor the interfacial diffusion of DHMBA monomer in the wavelength range of 200–800 nm. All membrane samples were rinsed with DI water and dried using a supercritical drying apparatus (EM CPD300, Leica Microsystems, Inc., Buffalo Grove, IL, USA) before characterization. The membrane surface zeta potential was determined using an electrokinetic analyzer (SurPASS^{III}, Anton Paar GmbH, Graz, Austria)

with 1 mM KCl as the electrolyte solution and the pH was adjusted using NaOH (0.1 M) and HCl (0.1 M) solutions. The surface morphology of each membrane was examined using FE-SEM. Each sample was coated with a thin layer of gold before examination. Surface roughness was analyzed for a 3 μm × 3 μm scanning range using an atomic force microscope (AFM, Multimode 8, Bruker, Billerica, MA, USA) in intelligence mode at ambient conditions. The thickness of the polymer layer was examined by laser ellipsometry (EMPro-PV, China) with an incidence angle of 70° in the ambient environment. Contact angles were measured using a contact angle measurement device (*KRÜSS* DSA30, Germany) with FAMAS Interface Measurement & Analysis System (version 3.1.3). The sessile drop method was used to measure the contact angle of a 20-μL water droplet placed carefully on the flat membrane surface. In total, eight measurements were carried out for each sample at different locations. Number- and weight-average molecular weights (M_n and M_w) were measured by gel permeation chromatography (GPC) on a Waters 1515 HPLC system (Waters Chromatography, Inc., USA) equipped with polystyrene gel columns and calibrated with standard polystyrene samples. The columns were eluted with DMF containing 0.05 M LiBr at a flow rate of 1.0 mL min^{-1}. Transmission electron microscopy (Hitachi H-7650, Japan) was used to observe the morphology of all membranes. Embedded samples were cut into 70 nm thick slices with a Leica Ultra Cryo UC7 microtome (Leica Mikrosysteme GmbH, Vienna, Austria) and placed on a copper grid (formvar/carbon, 300 mesh, Ted Pella, Inc., Redding, CA).

SUPPLEMENTARY TEXT

Fabrication of Polyester Membranes.

The chemical structure of DHBA is somewhat similar to that of *m*-phenylene diamine (MPD), regardless of the functional group types (Fig. 1A). However, as the pK_a values of common phenols are much greater than common anilines (*40*), the nucleophilicity of the former compounds is several orders of magnitude lower than that of the latter ones. Compared to DHBA, introducing a methyl group (equivalent to DHMBA) would further reduce the reactivity of the two phenolic groups toward the nucleophilic substitution reaction with TMC. GPC measurement confirmed this result, where the M_n of the DHMBA-based homopolymer (1719 Da) was lower than that of the DHBA-based one (2100 Da). Hence, a co-solvent-assisted IP method was utilized to promote the diffusion of phenolic monomers from the aqueous phase to the organic phase to react with TMC and form a polyester layer. The end-capping with IPC would not only provide additional dangling –COOH groups after hydrolysis but also react with residual –OH groups after the IP reaction. In addition, the incorporation of non-electron-rich acid may prevent undesired side reactions (e.g., chlorination) in the presence of an active chlorine solution.

Prior to the membrane fabrication, the molecular diffusion of DHMBA was monitored in situ by UV-Vis spectrophotometry (fig. S16). Extremely low absorbance was observed for DHMBA in alkane solvents (e.g., *n*-hexane) after a certain period, suggesting limited diffusion of the molecule. The low solubility of DHMBA in *n*-hexane and the significant polarity difference between them are responsible for this limited diffusion. Using pure chloroform resulted in enhanced molecular diffusion, as evidenced by the rapidly increasing absorbance. Performing IP with a mixed solution containing 20% (v/v) chloroform in *n*-hexane yielded a polyester membrane with satisfactory desalination performance.

A practical issue is the toxicity of chloroform, which led us to explore another organic solvent (ethyl acetate) with a similar polarity but lower toxicity than chloroform (*41*). As shown in fig. S16, the diffusion of DHMBA in ethyl acetate was slightly lower than in chloroform. Using a mixture containing 25% (v/v) ethyl acetate in *n*-hexane produced a similar absorbance curve to that of chloroform/*n*-hexane, corresponding to a diffusion rate of 0.8–1 mmol L^{-1} m^{-2} s^{-1}. This solvent condition in the IP process resulted in an RO membrane with slightly inferior desalination performance (3.28±0.39 L m^{-2} h^{-1} bar^{-1} water permeance and 96.1±0.3% NaCl rejection) to the SW30 membrane (fig. S17).

Calculation of Crosslinking Density of Polyester TFC Membranes.

For DHMBA membranes, each fully cross-linked structure provides 5 O and 16 C, whereas linear structures provide 6 O and 16 C (fig. S18). Due to the self-polymerization of the DHMBA molecule, its practical CD was calculated according to the following equation:

$$o \neq 0,\ p \neq 0,\ q \neq 0,$$

$$\frac{O}{C} = \frac{7m + 8n + 6o + 7p + 6q}{17m + 17n + 17o + 17p + 16q} \tag{S14}$$

$$CD = \frac{m + o}{m + n + o + p + q}$$

where *m* and *n* are defined in fig. S18. As o, p, and q are variable, the calculated CD was expressed as a range. Detailed data are summarized in table S2.

DFT Analysis of Chlorine Resistance of Two Proposed Structures.

We geometrically optimized the repeating units of the proposed monomers to verify the structure-property relationships of RO membranes regarding their chemcial reactivity (fig. S12). The HOMO and LUMO energies of two chemical structures were calculated to determine which atoms contribute to the frontier molecular orbitals. In general, the HOMO energy (E_{HOMO}) is associated with the ability of the molecule to donate electrons, whereas the LUMO energy (E_{LUMO}) indicates the ability of the molecule to accept electrons. Therefore, a greater E_{HOMO} indicates a higher tendency of the molecule to donate electrons toward electrophilic attack by radicals or atoms. As summarized in figs. S12 and S13, a slightly lower E_{HOMO} of -6.54 eV and a higher E_{LUMO} of -2.73 eV were obtained for DHMBA, whereas -6.50 and -2.83 eV were obtained for DHBA (E_{HOMO} and E_{LUMO}). As a result, the greater energy gap of the DHMBA molecule (table S1) verifies its greater inertness, which is also proven experimentally.

Subsequently, we analyzed the Mulliken population to investigate the specific atomic charge of each molecule by assuming complete Cl substitution at the possible sites (table S1). Here, a positive Mulliken population represents the loss of electrons, while negative values refer to the enrichment of electrons relative to free atoms. Low negative values were given to carbons (C1 and C3, labled in fig. S12) in DHMBA, indicating the low probability of the Cl substitution at the benzene ring. This result was further supported by Fukui function values (f_k^-). The two carbons in DHMBA exhibited similar values to those in DHBA (table S1), indicating the same low potential of the two structures to be attacked by an electrophile.

Experimental Analysis of Chlorine Resistance of DHMBA Membranes at High pH Conditions.

Owing to the polyester chemistry, both PIP-DHBA-DHBA (as reported in ref. *9*) and DHMBA membranes exhibited stable operation in the presence of chlorine in acidic and neutral pH conditions. Note that the unique structure of the DHMBA membrane could afford long-term stability at pH 9.0, while the DHBA membrane started to degrade at pH 8.0. However, we still observed performance decline of the DHMBA membrane with increasing the solution pH above 10 (fig. S32). While the DFT results revealed a high energy barrier for the DHMBA/TMC structure to be attacked by OH^-, it underwent a similar energy release as the DHBA/TMC structure once the OH^- had attacked the ester carbon site (fig. S33). The bond dissociation energy of the ester linkage was also found to be rather close for the two representative units (1.99 vs. 2.04 eV, table S1). These calculations suggest similar structural deformation for both membranes. We suggest avoiding exposure of the polyester RO membranes to highly alkaline conditions for long-term operation.

Gypsum Scaling Propensity of the RO Membranes.

The gypsum scaling experiments were conducted with two separate solutions: (i) model $CaSO_4$ solution at a saturation index (SI) of 0.51 and (ii) simulated seawater with a calculated SI of 0.52. As the operational water flux greatly influences the scaling potential of the membranes, the initial water fluxes of membranes were manually adjusted to be identical across experiments depicted in Fig. 3A and 3B. In both tests, the SW30 membrane experienced a fast decline in water flux with time. In contrast, no performance decline was observed for the DHMBA membrane in both tests. We note that although the bulk solution SI was lower than 1, the SI on the membrane surface was much higher (~ 3.58 for Fig. 3A and ~1.63 for Fig. 3B) because of the severe concentration polarization when operating at high water fluxes (110 L m^{-2} h^{-1} in Fig. 3A and 50.6 L m^{-2} h^{-1} in Fig. 3B).

The abundant carboxylic acid groups on the polyamide (SW30) RO membrane surface, which form Ca^{2+} complexes, and the much higher surface roughness could be responsible for the enhanced heterogeneous nucleation of gypsum crystals (*42*). The carboxylic acid group in the DHMBA molecule was primarily consumed during the self-polymerization, which resulted in a lower negative surface charge (see zeta potential data in fig. S30 and estimated surface

carboxyl group density from the silver binding method in fig. S31). In addition, the surface of the polyamide membrane is more hydrophobic than the DHMBA membrane (fig. S34), which lowers the energy barrier for heterogeneous nucleation (*42*). These factors are responsible for the severe scale formation of the SW30 membrane, as shown in the FE-SEM images (Fig. 3E and 3F). The accumulation of microcrystals formed several aggregates and a corresponding cake layer on the surface of the SW30 membrane.

To further understand the antiscaling performance of the DHMBA membrane, QCMD measurements were conducted. As shown in Fig. 4B and 4C, both DHMBA and SW30 membranes showed mass accumulation on the membrane surface when the gypsum solution was injected into the chamber. For the model gypsum solution with an SI value of 0.51 (Fig. 4B), the SW30 membrane showed much higher mass accumulation. We note that the mass accumulation in these experiments is contributed by both the adsorbed ions as well as any scale that forms by heterogenous neucleation. Moreover, the scaled SW30 membrane was unable to recover its original mass after cleaning with DI water, suggesting an irreversible accumulation of mass on the membrane surface. In contrast, the DHMBA membrane showed only a slight increase in mass adsorption and could readily regenerate to its pristine state. Using simulated seawater as the feed, the solution complexity did not alter the scaling resistance of the DHMBA membrane either, as revealed by the rather gentle mass increase (Fig. 4C). In comparison, the SW30 membrane exhibited considerable mass increase within a short period, suggesting high vulnerability to gypsum scaling.

Antifouling Properties of the RO Membranes.

Organic fouling experiments were conducted with two typical model foulants (sodium alginate, SA, and humic acid, HA). As before, the initial water fluxes of both membranes were kept constant to eliminate hydrodynamic differences, which affect membrane fouling (*43*). In brief, only ~1% flux decline was observed for the DHMBA membrane by the end of the test (model seawater with SA), whereas a sharp decrease of up to 37% was observed for the SW30 membrane (Fig. 3C). Slightly more fouling occurred when HA was used as the foulant, as indicated by the 8% flux decline for the DHMBA membrane (Fig. 3D). In contrast, only 50% of the initial flux was retained for the SW30 membrane after 24 hours of operation (Fig. 3D). Surface FE-SEM images further verified the fouling states of the two membranes (Fig. 3G, 3H, 3K, and 3L). Thick and compact cake layers were identified on the surface of the SW30 membrane, which reasonably explained the sharp flux decline. In comparison, the surface of the DHMBA appeared clear (SA solution) or with dispersed aggregates (HA solution) by the end of each test.

The excellent antifouling property of the DHMBA membrane could be attributed to its unique surface physicochemical properties. First, conventional polyamide RO membranes possess significant roughness with a ridge-and-valley surface morphology (fig. S20). Such a rough surface facilitates the deposition of foulants on the membrane. In comparison, the DHMBA membrane exhibits a smoother surface (Fig. 1D), which foulants find more difficult to adhere to under a crossflow shear force. Second, the higher carboxyl group density on the surface of the polyamide membrane, as indicated by its more negative zeta potential (fig. S30), results in higher organic fouling due to the bridging of organic foulants to the surface carboxyl groups by calcium ions (*36*, *44*). Last, the DHMBA membrane has a lower surface energy than the polyamide membrane (fig. S34) after taking the surface roughness into consideration. Studies have shown that an active layer with low surface energy allows adhered organic foulants to be easily washed away by hydrodynamic shear induced by the cross-flow (*45*).

Boron Removal Mechanism of Polyester TFC Membranes.

Boric acid is a weak acid with pK_{a1}≈8.6 in seawater (*40*). Since most seawater used in desalination has a pH of 7.5–8.5, boric acid is mainly uncharged, leading to unsatisfactory rejection of conventional polyamide RO membranes. Compared to the rejection of boron by the SW30 membrane (74.4±0.8%), a much higher rejection (93.2±0.3%) was obtained for the DHMBA membrane. A similar result was obtained for the PIP-DHBA-DHBA membrane (92.3±0.2%), suggesting the ability of polyester membranes to highly reject boron.

Despite the slightly higher salt rejection of the SW30 membrane compared to the DHMBA membrane, the boron rejection of the DHMBA membrane is substantially higher (Fig. 1H). We note that the estimated effective pore radii of the DHMBA and SW30 membranes are comparable (0.289 and 0.286 nm, respectively, fig. S29). We attribute the difference in the boron rejection behavior of the RO membranes to their chemistry and charge characteristics. The higher carboxyl group density on the surface of the SW30 membrane (figs. S30 and S31) likely enhances the partition of boric acid molecules into the membrane via hydrogen bonding. After partitioning, the boric acid molecules experience higher friction in the DHMBA than the SW30 membrane due to interaction with carboxyl groups which are more abundant in the DHMBA membrane (fig. S31B), thereby hindering the diffusion of boric acid through the membrane. Thus, the lower partitioning of boric acid to the DHMBA membrane and the higher friction within the membrane matrix can explain its higher boric acid rejection.

Analysis of Adhesion Forces of the RO Membranes.

AFM was used to evaluate the adhesion forces between organic foulants and the membranes, as the membrane fouling rate and the adhesion forces are correlated (*36*). In Fig. 4A, the normalized adhesion force, i.e., F_{max} (maximum adhesion force) divided by R_p (the radius of carboxyl-modified particles probe), serves as an indicator for the fouling propensity of membranes. For the polyester (DHMBA) RO membrane, the adhesion forces were smaller (i.e., less negative or less adhesive) compared to the SW30 membrane. Specifically, the average adhesion force was -3.3 mN m^{-1} for the SW30 membrane (more negative value means more adhesive) compared to -0.89 mN m^{-1} for the DHMBA membrane. The lower adhesion fore for the DHMBA membrane is attributed to its lower density of –COOH groups (fig. S31), smoother surface (Fig. 1D), and lower surface energy (fig. S34 and table S8) compared to the SW30 membrane.

APT Analysis of the RO Membranes.

The element composition of both SW30 and DHMBA membranes was detected using APT technology. The extremely low-density regions in the analyzed volumes of the SW30 and DHMBA membrane structures could be revealed with iso-density surfaces at the semi-peak density of each dataset (fig. S26). We observed a notable low-density structural region (potentially a cavity) in the SW30 model, whereas the DHMBA membrane appears to be comparatively intact. The irregular cavity observed in the three-dimensional reconstruction of the SW30 membrane is highly likely to be a section of a nanobubble on the surface of the active layer. The discrepancy between these two membranes originates from the thermodynamics and kinetics in the IP process for fabricating TFC membranes. The exothermic nature of the IP process generates Rayleigh-Bénard convection (*46*), leading to the initial bending and collapse of the thin film. It is evident that amino monomers exhibit higher reactivity compared to phenolic monomers. Under the same conditions, amino monomers undergo a more intense reaction and release more heat, exacerbating thermal instability, which is manifested macroscopically as an increased presence of nanobubbles (*46*). The formation of these nanobubbles resulted in the rough surface of the SW30 membrane (consistent with AFM results) and contributed to its poor resistance to fouling. In contrast, the smooth surface of the DHMBA membrane enhances its resistance to fouling.

Analysis of ToF-SIMS of the RO Membranes.

For the SW30 membrane, the signals for typical fragments including $–C_7H_3O_2$, $–C_7H_5ON$, and –CN–, denoting benzoate, benzamide, and amide, respectively, decreased from the beginning of the test (fig. S27), suggesting the decomposition of polyamide chemistry. By contrast, the $–SO_2–$ curve, which was derived from the polysulfone substrate (*47*), was found to increase inversely. A similar tendency was also observed for the DHMBA membrane, where signals for typical polyester segments (i.e., tribenzoate, $–C_9H_3O_6$; hydroxyl-methyl-benzoate, $–C_8H_6O_3$) declined sharply at the initial state. More interestingly, apparent boundary regions could be distinguished for both membranes. For instance, the median intensity for all signals was located at ~100 nm in depth for the SW30 membrane, in contrast to 30–50 nm for the DHMBA membrane. In their 3D and cross-sectional fragment images, a much clearer concentration gradient was identified for the commercial membrane, compared to the limited incident depth for the polyester membrane. The ToF-SIMS results were consistent with the observations from the TEM images (fig. S19) and Ellipsometry characterizations (table S3), which were also in good agreement with the high water permeances observed in performance testing.

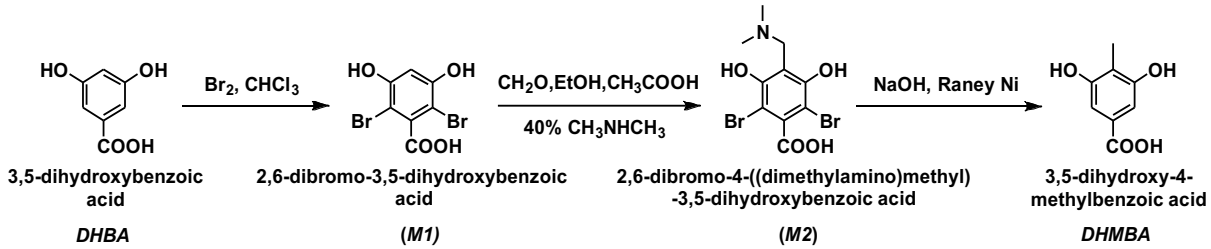

Fig. S1. Synthetic route for DHMBA.

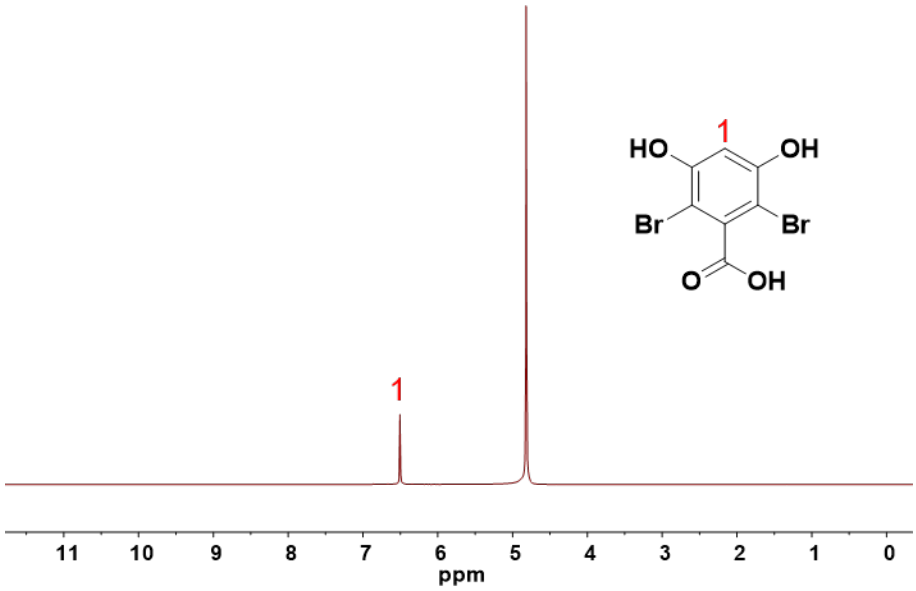

Fig. S2. ^{1}H NMR spectrum of 2,6-dibromo-3,5-dihydroxybenzoic acid (***M1***, D_2O).

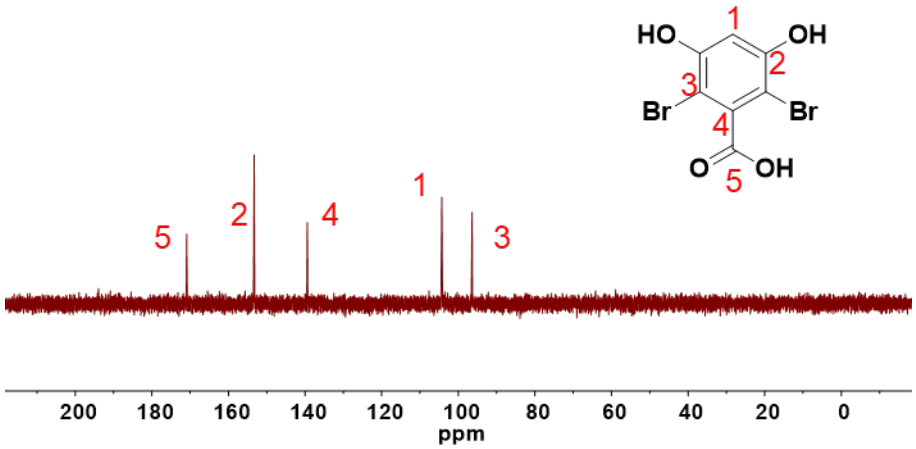

Fig. S3. ^{13}C NMR spectrum of 2,6-dibromo-3,5-dihydroxybenzoic acid (***M1***, D_2O).

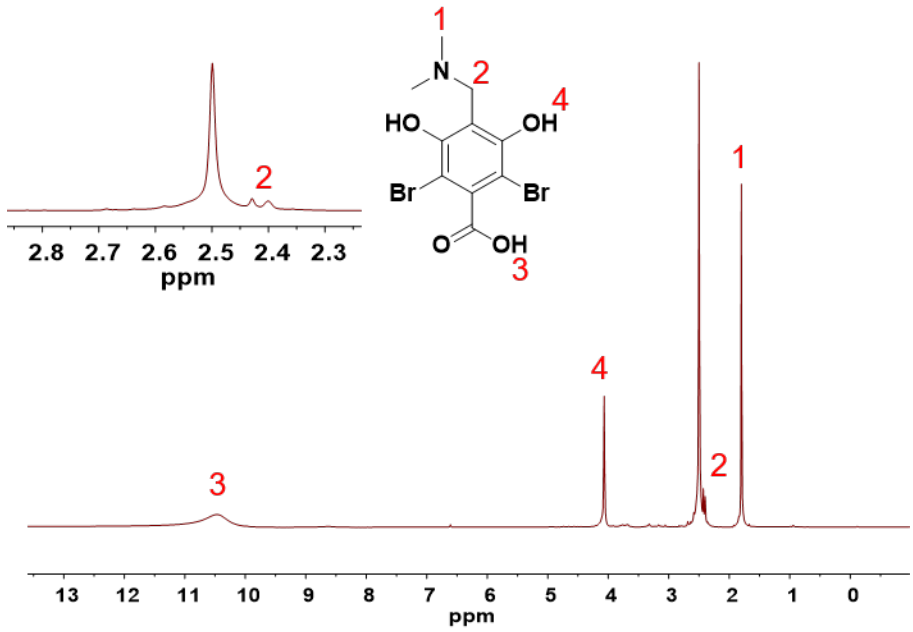

Fig. S4. ^{1}H NMR spectrum of 2,6-dibromo-4-((dimethylamino)methyl)-3,5-dihydroxybenzoic acid (***M2***, DMSO-d_6).

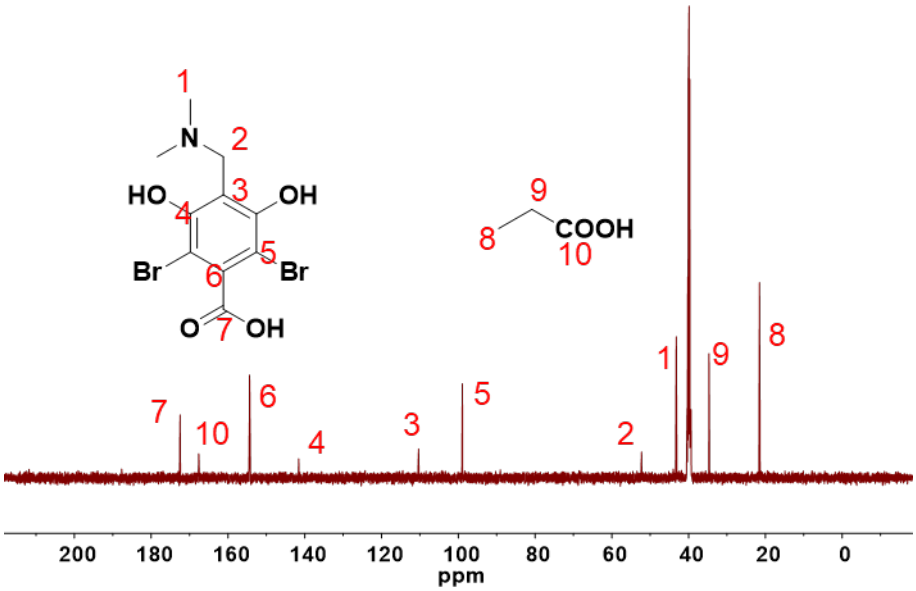

Fig. S5. ^{13}C NMR spectrum of 2,6-dibromo-4-((dimethylamino)methyl)-3,5-dihydroxybenzoic acid (***M2***, DMSO-d_6). The impurity (acetic acid) was also labeled in the spectrum.

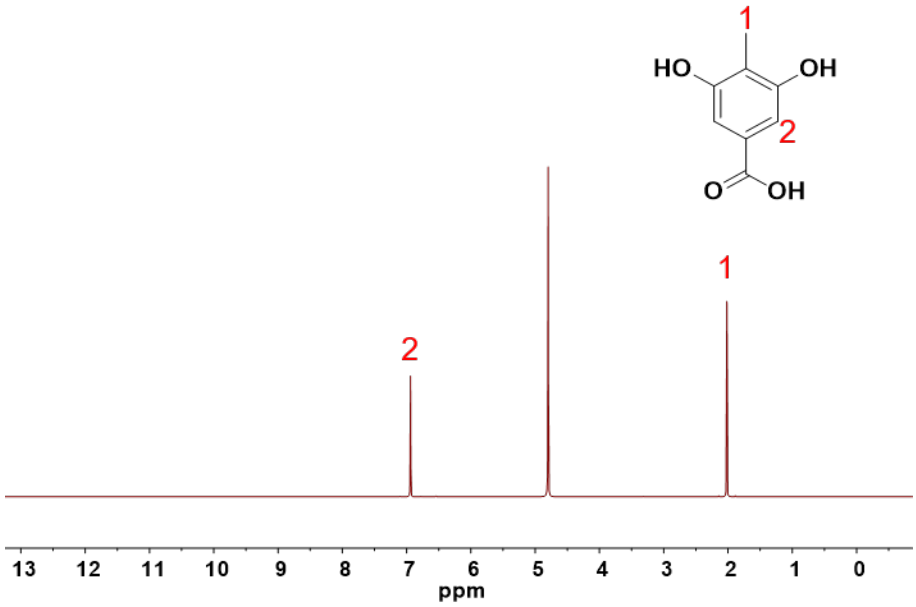

Fig. S6. ^{1}H NMR spectrum of 3,5-dihydroxy-4-methylbenzoic acid (***DHMBA***, D_2O).

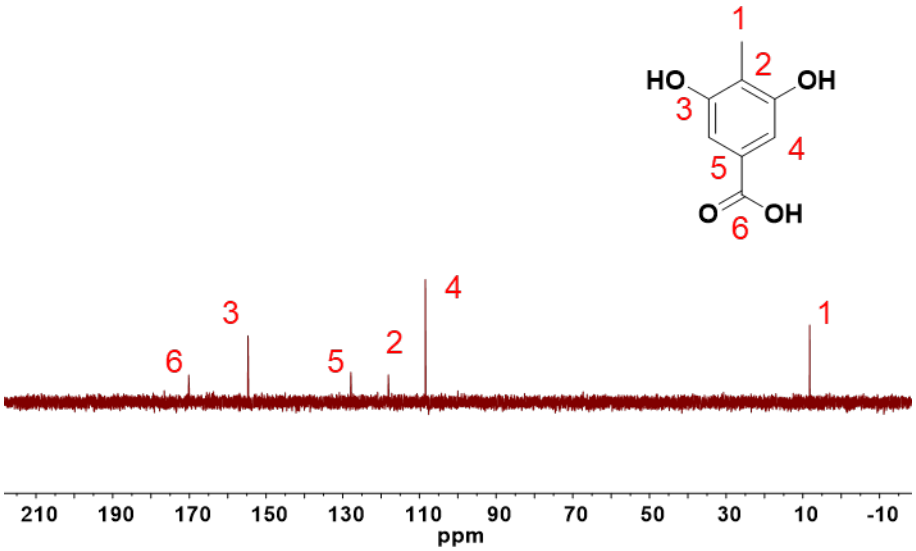

Fig. S7. ^{13}C NMR spectrum of 3,5-dihydroxy-4-methylbenzoic acid (***DHMBA***, D_2O).

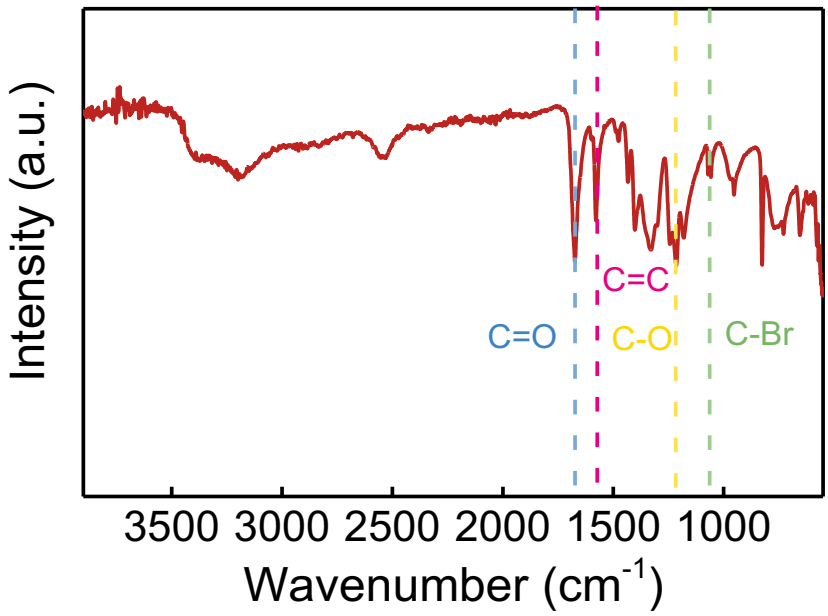

Fig. S8. FTIR spectrum of 2,6-dibromo-3,5-dihydroxybenzoic acid (***M1***).

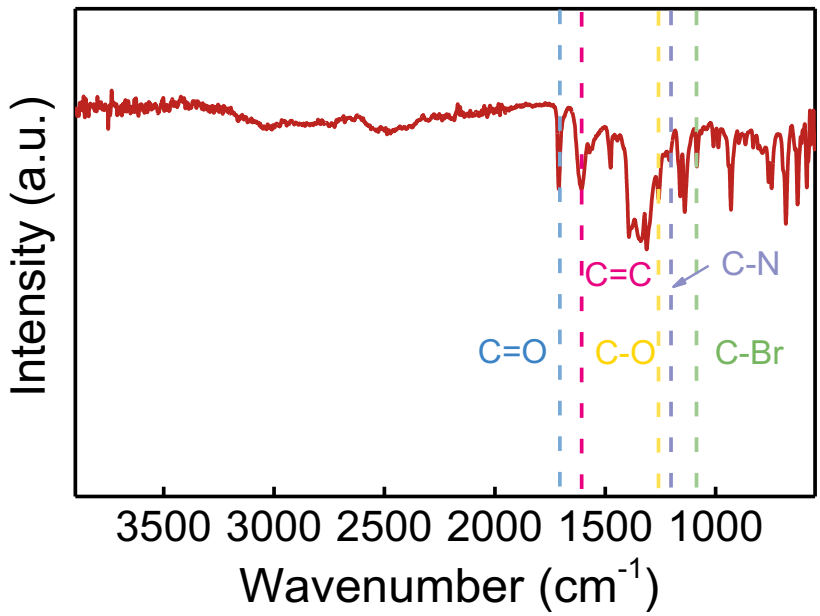

Fig. S9. FTIR spectrum of 2,6-dibromo-4-((dimethylamino)methyl)-3,5-dihydroxybenzoic acid (***M2***).

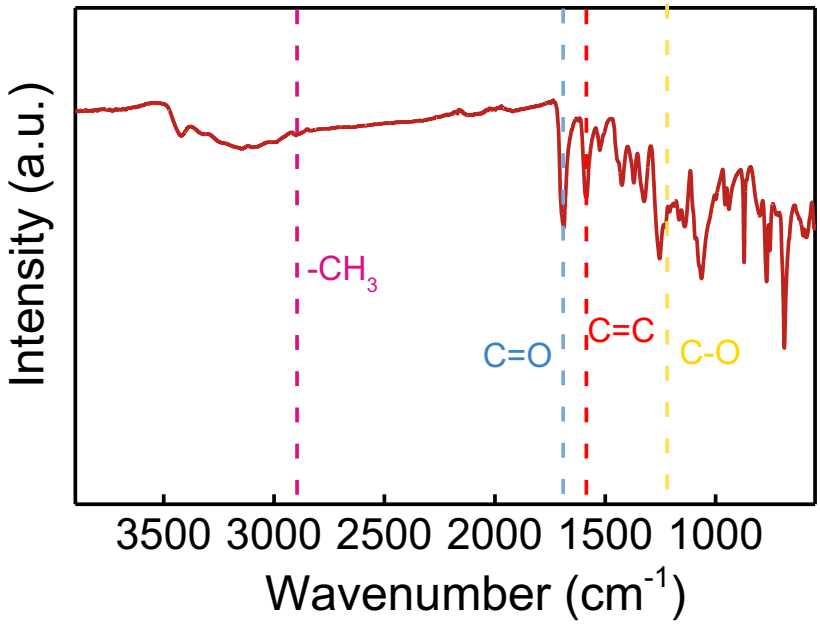

Fig. S10. FTIR spectrum of 3,5-dihydroxy-4-methylbenzoic acid (***DHMBA***).

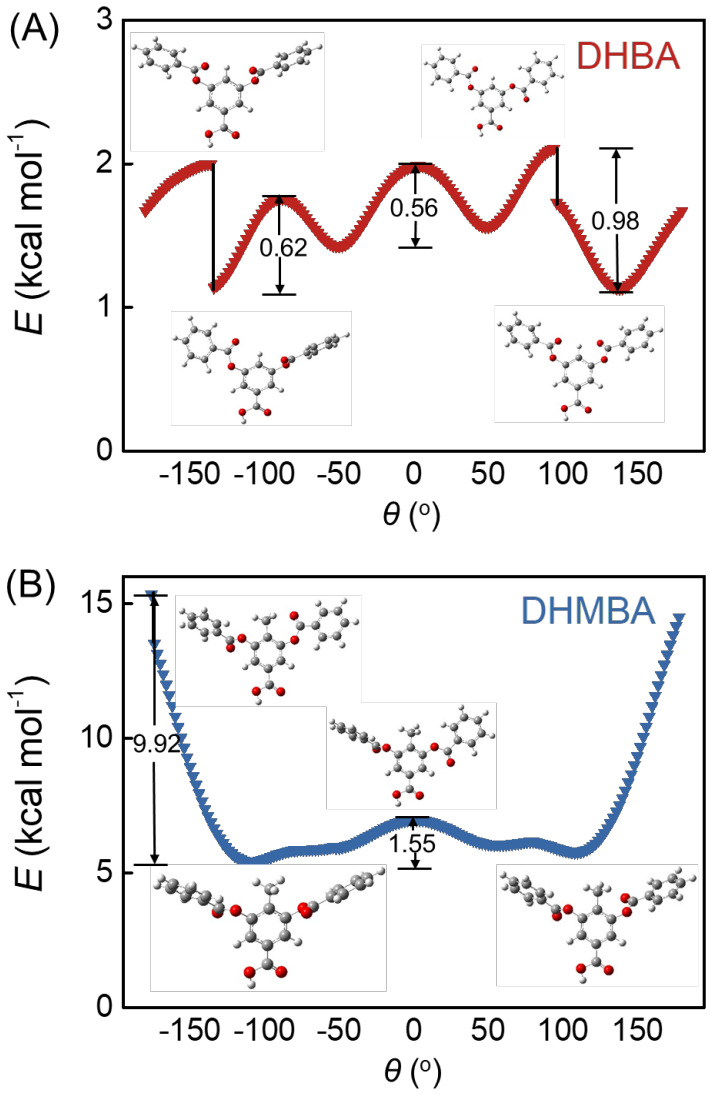

Fig. S11. Distribution of torsion angle (θ) for (A) DHBA and (B) DHMBA-based model compounds toward the attack by hydroxyl ions. The θ was defined as the angle between the plane consisting of C3, C4, and O1 atoms and the plane consisting of C4, O1, and C5 atoms in both structures (see structures in fig. S12).

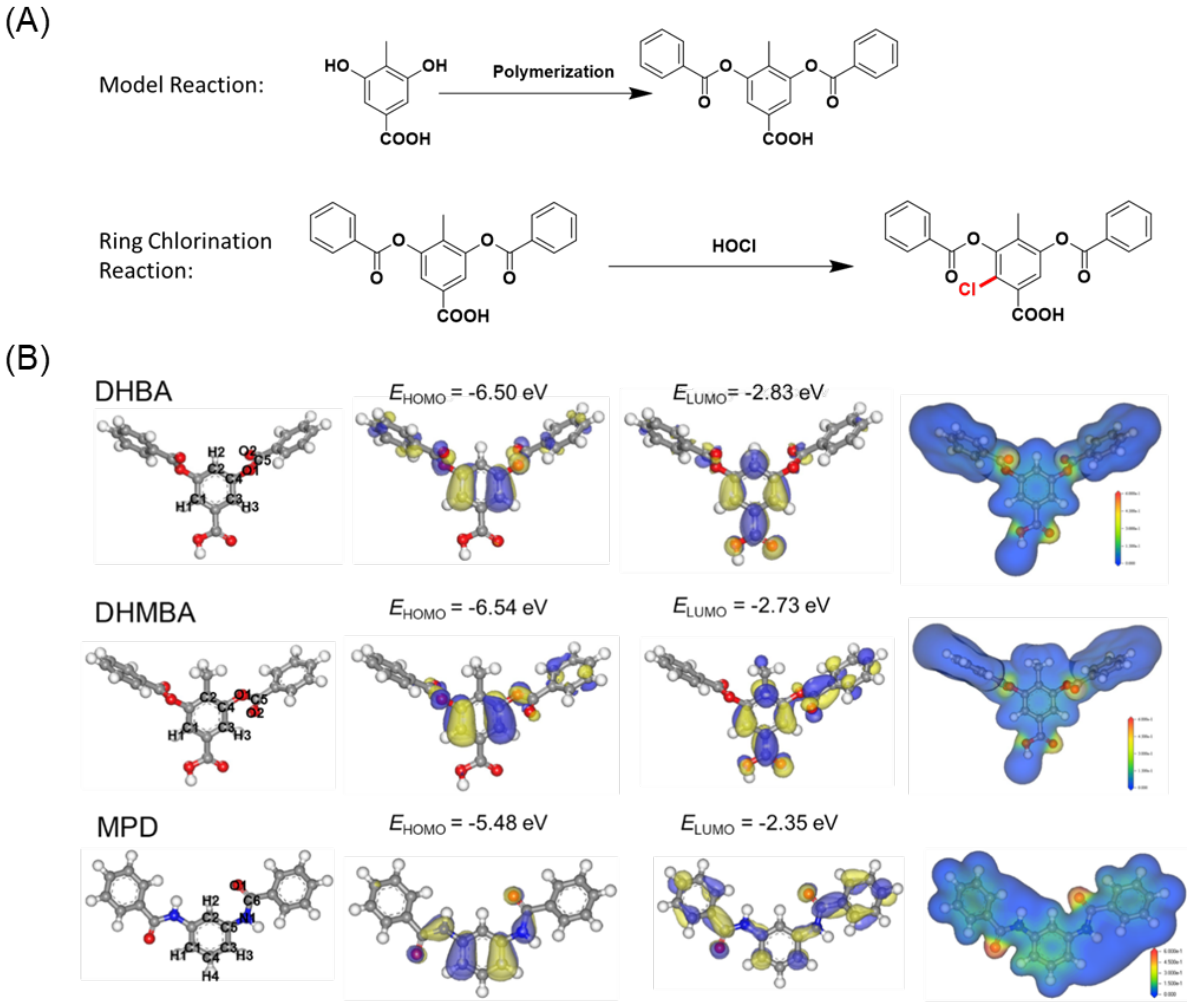

Fig. S12. (A) The self-polymerization of DHMBA and the ring chlorination reaction of the DHMBA-based model compound. (B) Images of the molecular orbitals of DHBA, DHMBA, and MPD repeating units, their corresponding HOMO and LUMO energy levels, and electron density profiles.

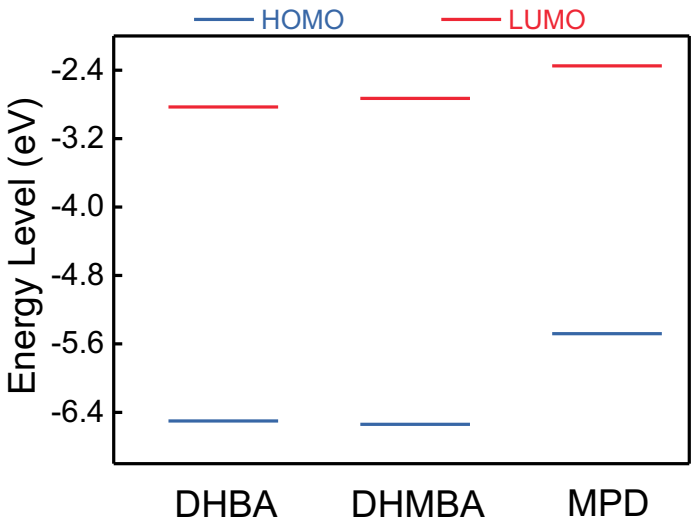

Fig. S13. Summary of HOMO and LUMO energies of DHBA, DHMBA, and MPD repeating units.

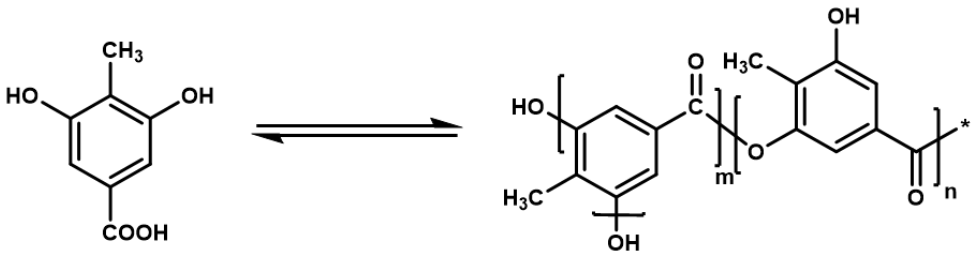

Fig. S14. Schematic illustration of the self-polymerization pathway of the DHMBA molecule.

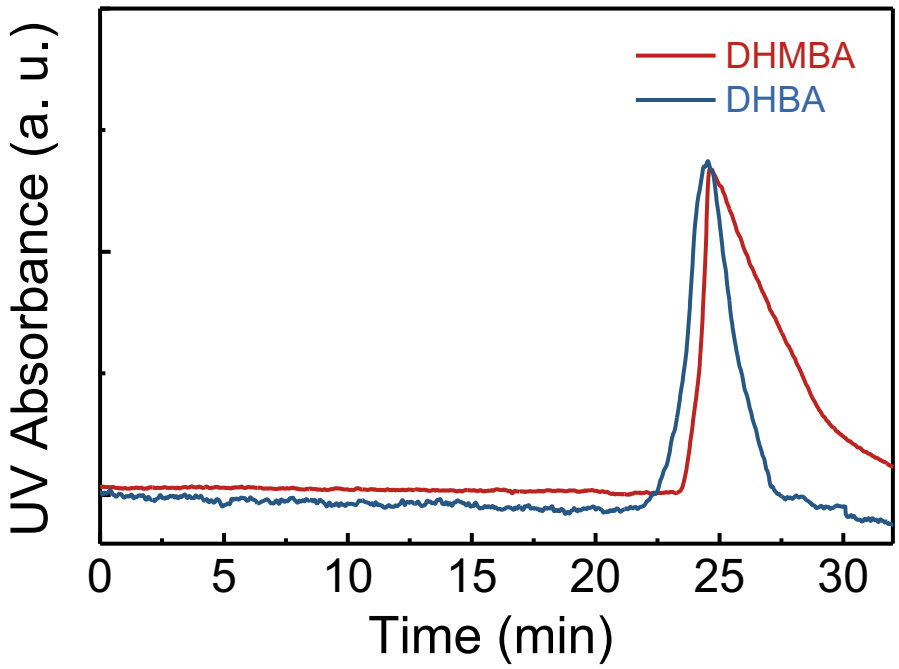

Fig. S15. GPC curves of the polymerization product of DHMBA and DHBA molecules. For DHMBA, 4.00 g DHMBA and 1.44 g NaOH were dissolved in 100 mL DI water (pH ~ 12), while 2.00 g DHBA and 1.56 g NaOH were dissolved in 100 mL DI water (pH ~ 12.5). Both solutions were stirred at room temperature for two minutes and then adjusted to neutral pH by adding HCl (aq.). After that, the solvent was evaporated using a rotary evaporator to produce a solid product.

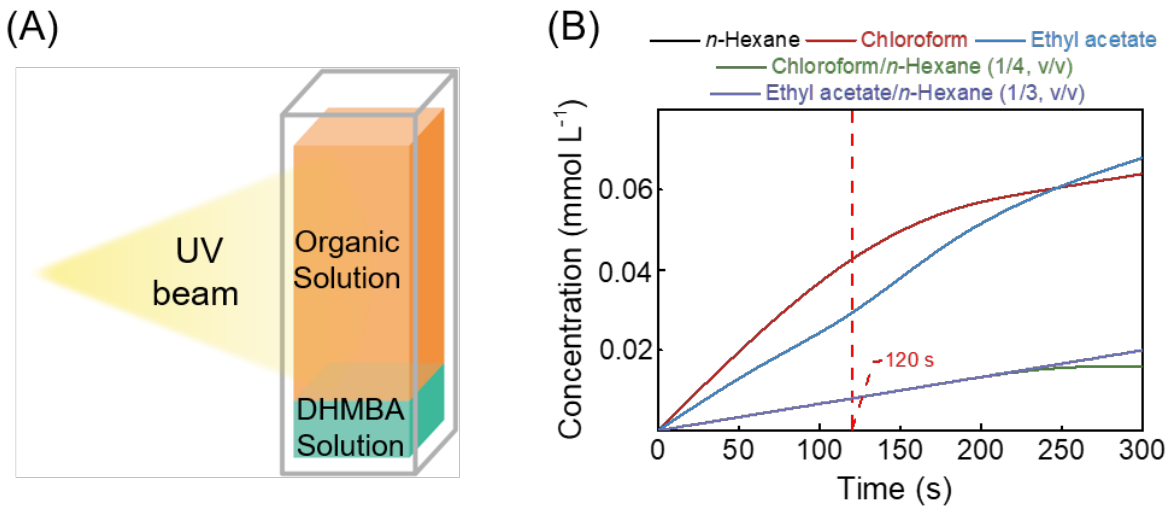

Fig. S16. (A) Schematic illustration of in situ monitoring of interfacial diffusion by UV-Vis spectrophotometry in a fixed quartz cuvette. (B) The detected concentration of DHMBA molecules with time. Here, the absorbance of DHMBA in the *n*-hexane solution was extremely low (nearly zero), compared to other solvents. For the experiments, 0.5 mL of the aqueous solution containing 20 mg DHMBA was initially placed in a quartz cuvette to ensure the liquid-air interface was right below the light source (about 30 μm). The absorbance data were immediately collected after carefully pouring 2 mL of organic solvent onto the top of the aqueous solution. Here, the organic solvents include *n*-hexane, ethyl acetate, chloroform, chloroform/*n*-hexane (1/4, v/v), and ethyl acetate/*n*-hexane (1/3, v/v). The experiments were recorded at a maximum absorption wavelength of 258 nm, a sampling interval of 0.5 s, and a test duration of five minutes using the kinetic mode in UV probe software.

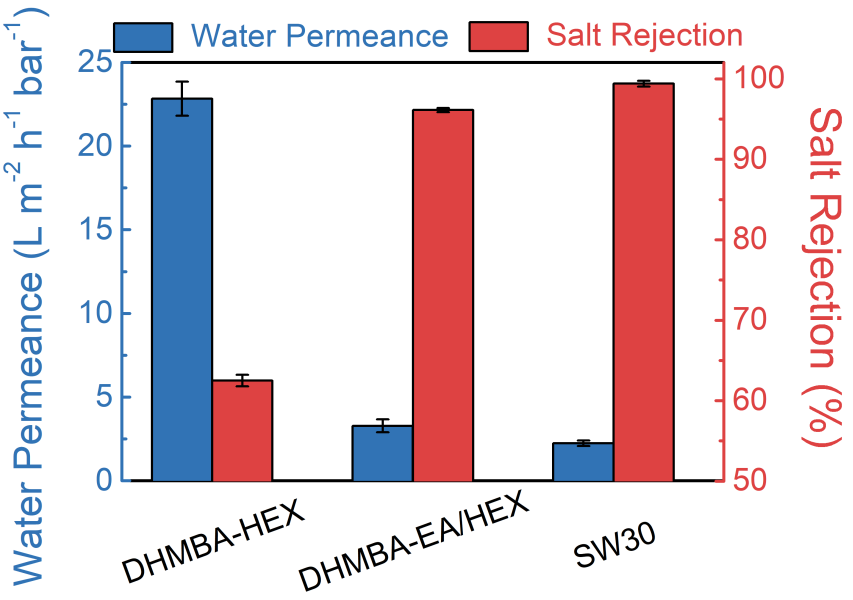

Fig. S17. Separation performance of DHMBA-based membranes compared to a commercial polyamide SW30 membrane. DHMBA-HEX, and DHMBA-EA/HEX refer to the membranes fabricated by conventional IP with pure *n*-hexane as the sole organic solvent and conventional IP with ethyl acetate/*n*-hexane (1/3, v/v) as the organic solvent, respectively. Here, EA and HEX denote the ethyl acetate and *n*-hexane used for the membrane fabrication. Membrane coupons (15.0 cm^2) were tested using a constant pressure of 15.5 bar, temperature of 25±0.5 ^oC, 2,000 mg L^{-1} NaCl feed solution, and crossflow velocity of 40.0 cm s^{-1}.

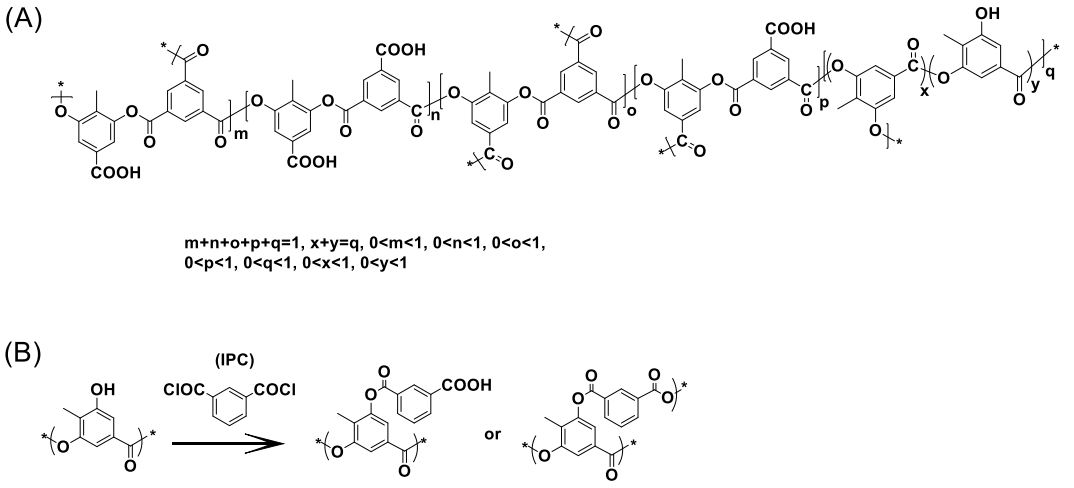

Fig. S18. (A) Polymeric structures of the DHMBA polyester membrane. Because five possible repeating units exist for the DHMBA membrane, its chemical structure was specified into five parts. Specifically, m and n represent the cross-linked and linear structure of DHMBA with TMC, respectively; o and p represent the self-polymerized DHMBA molecule coupled with cross-linked TMC and the self-polymerized DHMBA molecule coupled with linear TMC, respectively; and q represents the self-polymerized DHMBA molecule (q comprises a cross-linked moiety, defined as x, and a linear moiety, defined as y. (B) Reaction pathway of isophthaloyl dichloride (IPC) with the residual –OH groups in the polyester matrix. After the end-capping reaction, the residual –COCl groups would hydrolyze into –COOH groups or react with other –OH groups (through a coupling reaction).

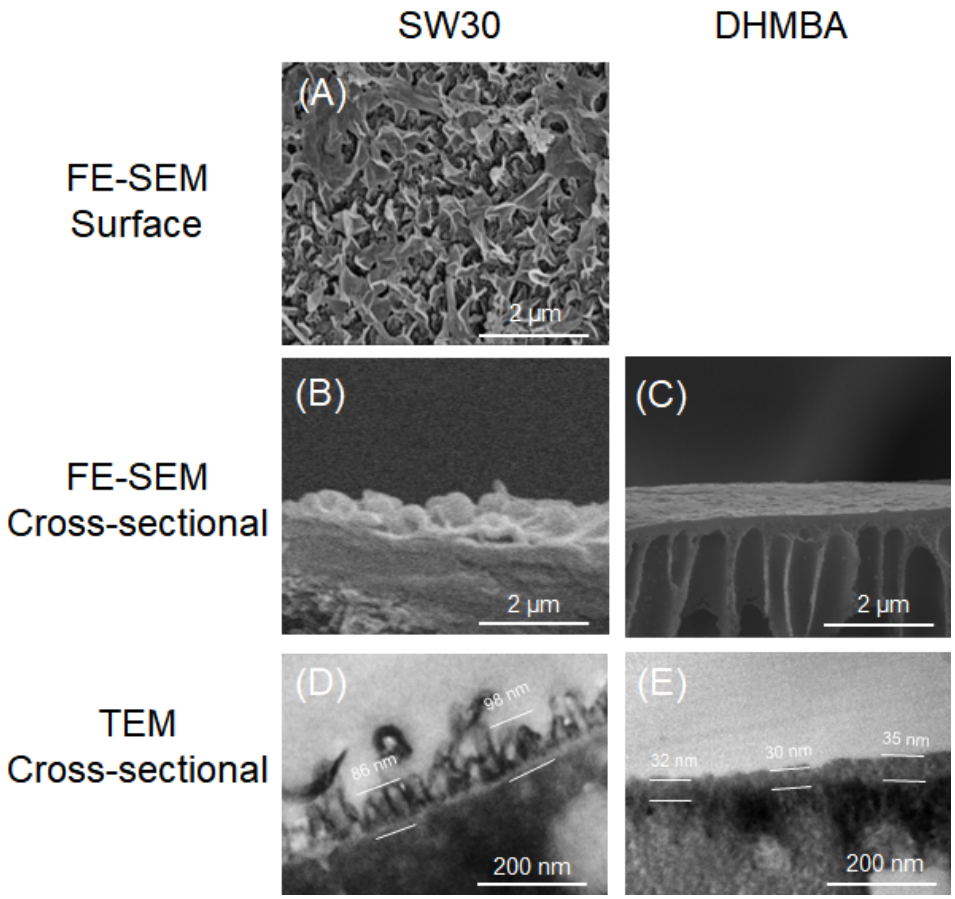

Fig. S19. Microscopic morphologies of the SW30 and DHMBA membranes. FE-SEM images of the top surface of (**A**) SW30 membranes. FE-SEM images of the cross-sections of (**B**) SW30 and (**C**) DHMBA membranes. Cross-sectional TEM images of (**D**) SW30 and (**E**) DHMBA membranes. The FE-SEM image of the top surface image of the DHMBA membrane is shown in Fig. 1 in the main text, demonstrating a much smoother surface than the SW30.

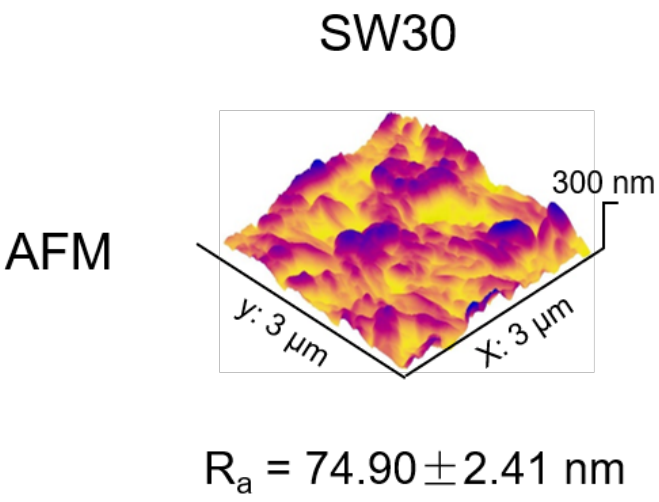

Fig. S20. AFM image and average surface roughness of the SW30 membrane.

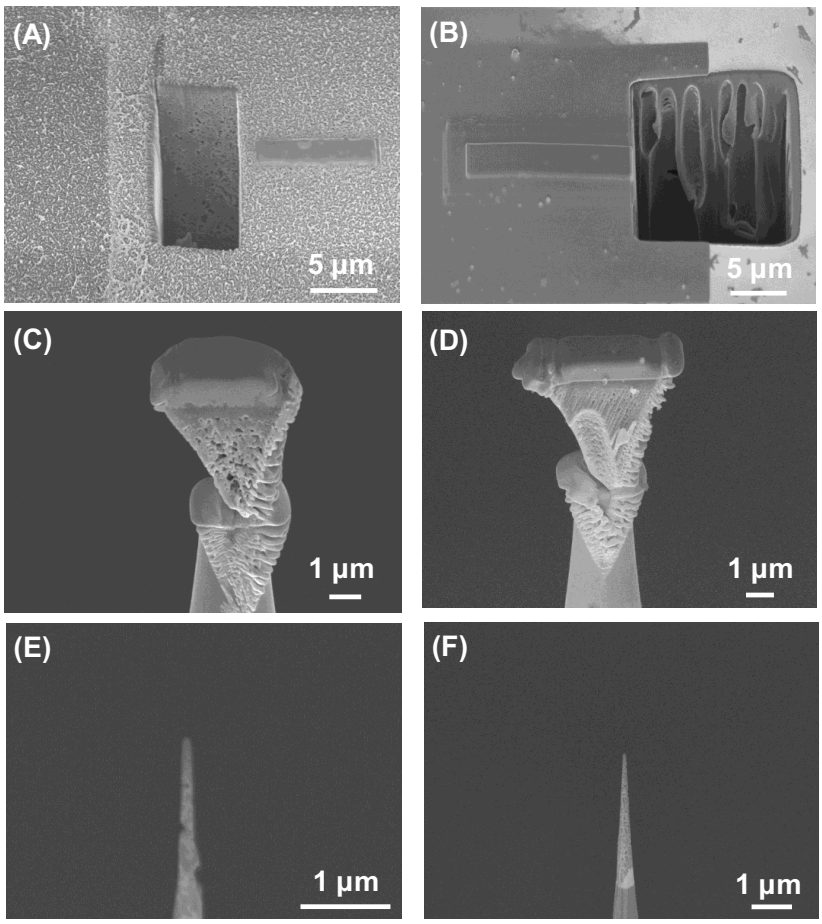

Fig. S21. The cut sampling images of (A) the SW30 membrane and (B) the DHMBA membrane during the preparation of APT needle-shaped specimens. Images of (C) the SW30 and (D) the DHMBA membrane samples on the silicon array. APT needle-shaped specimens of (E) the SW30 membrane and (F) the DHMBA membrane.

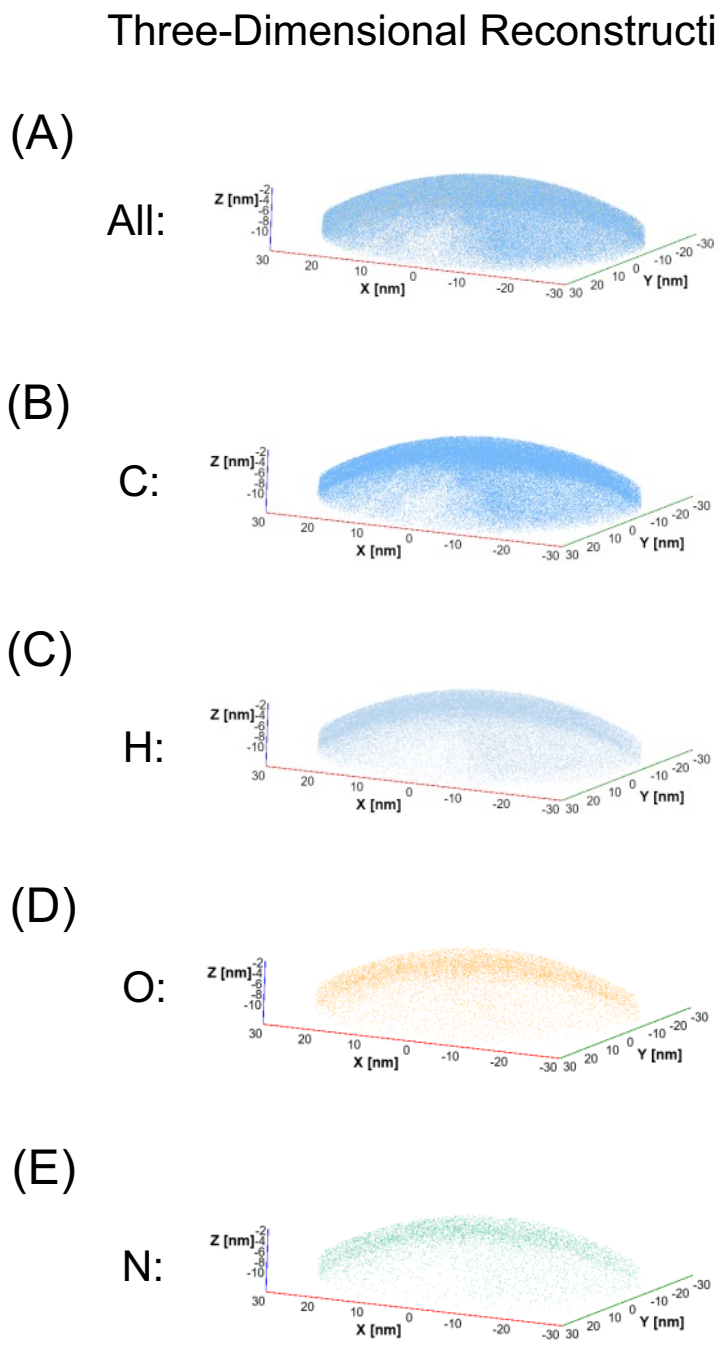

Fig. S22. Three-dimensional reconstructed atom maps of all elements (A), and single element of C (B), H (C), O (D), and N (E) from an APT dataset of the SW30 sample.

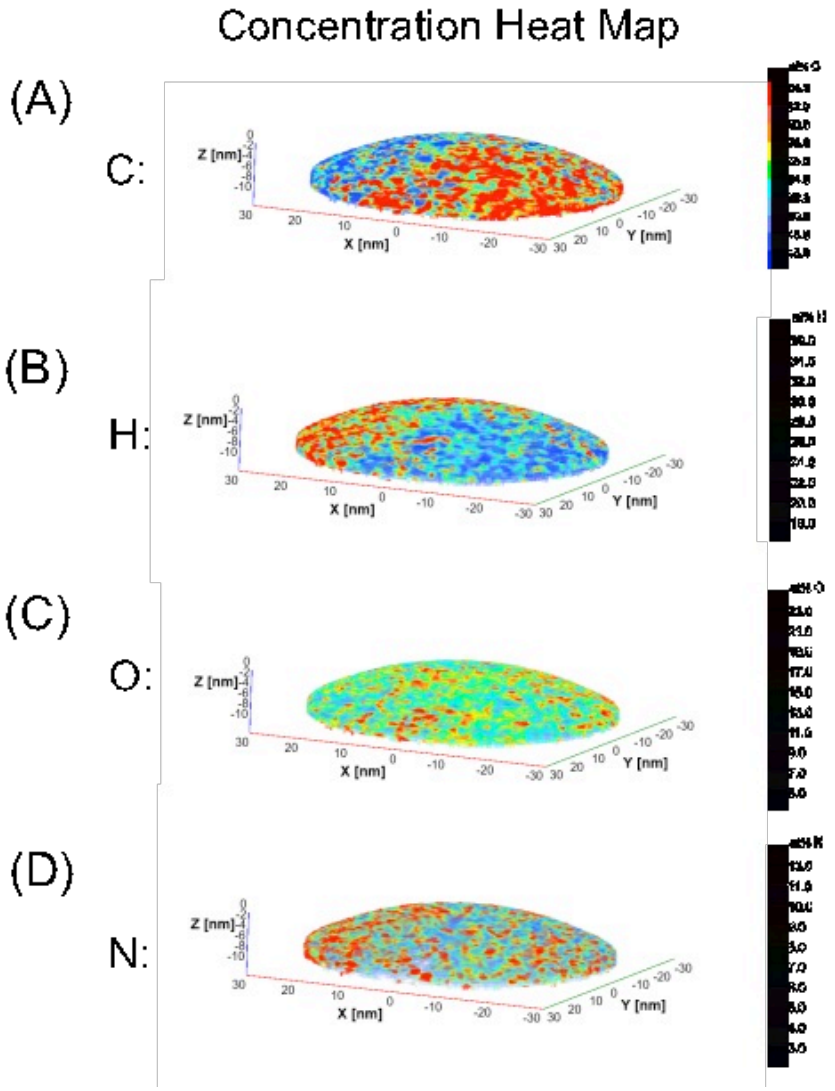

Fig. S23. (A, B, C, and D) Corresponding concentration heat of C, H, O, and N atoms, respectively, in the analyzed volume of the SW30 membrane.

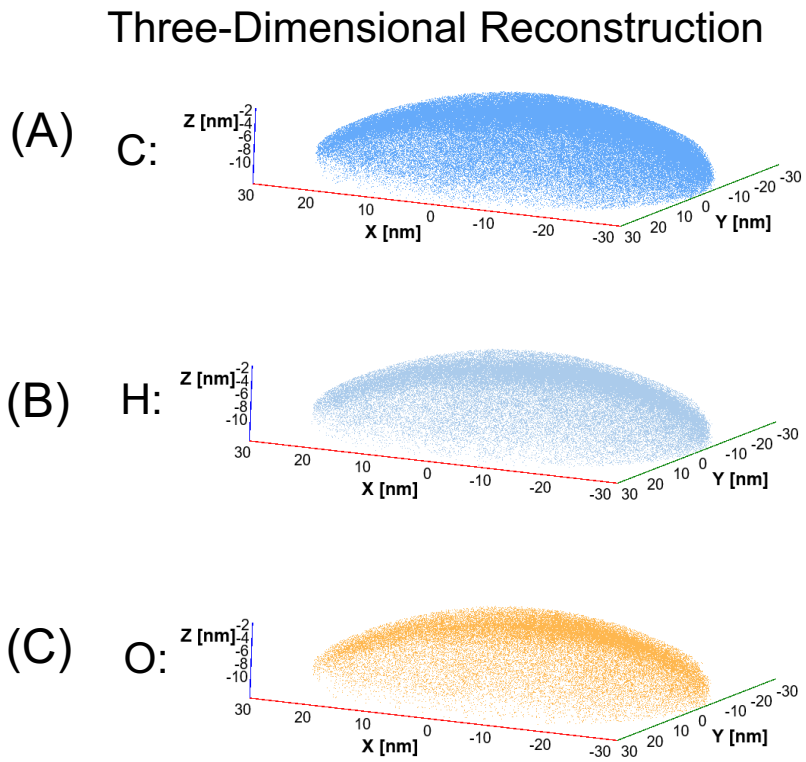

Fig. S24. Single element of C (A), H (B), and O (C) from an APT dataset of the DHMBA sample.

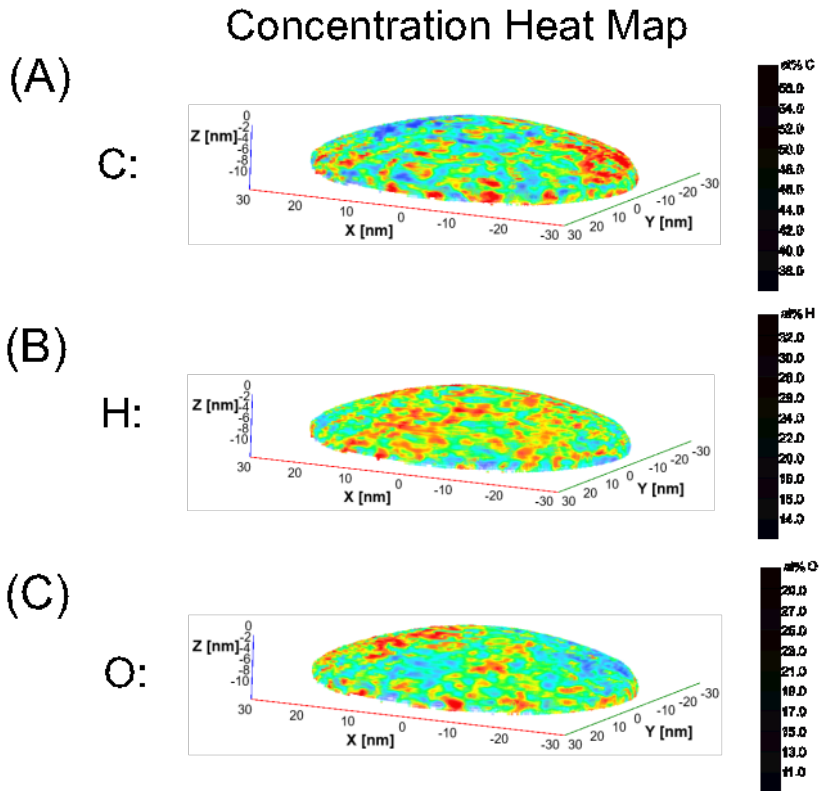

Fig. S25. (A, B, and C) Corresponding concentration heat of C, H, and O atoms, respectively, in the analyzed volume of the DHMBA membrane.

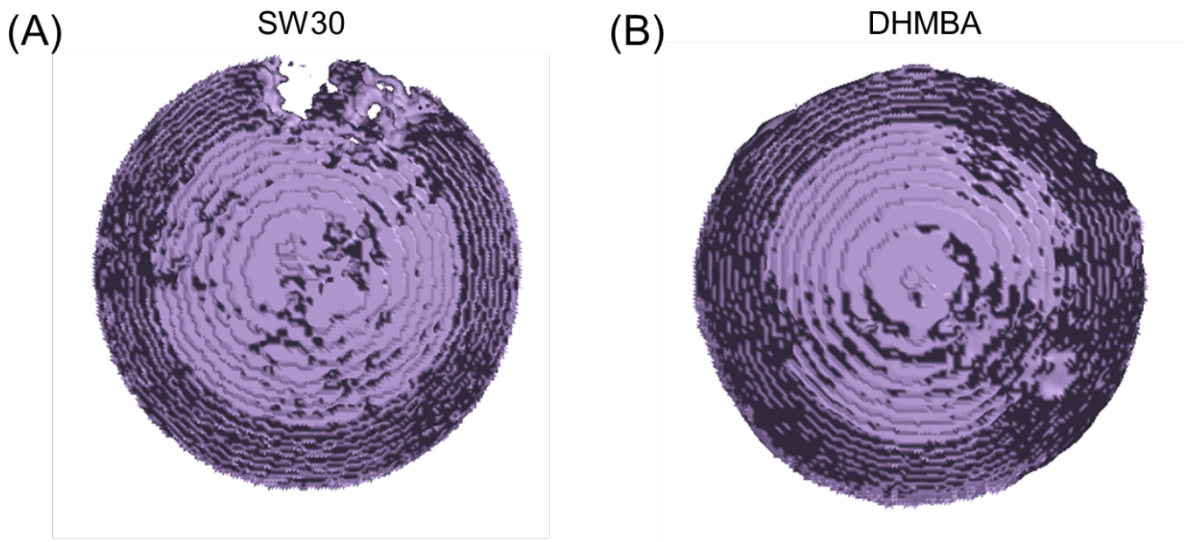

Fig. S26. The reconstructed volume of the (A) SW30 and (B) DHMBA membrane samples viewed with a low-density iso-surface at half of the peak density.

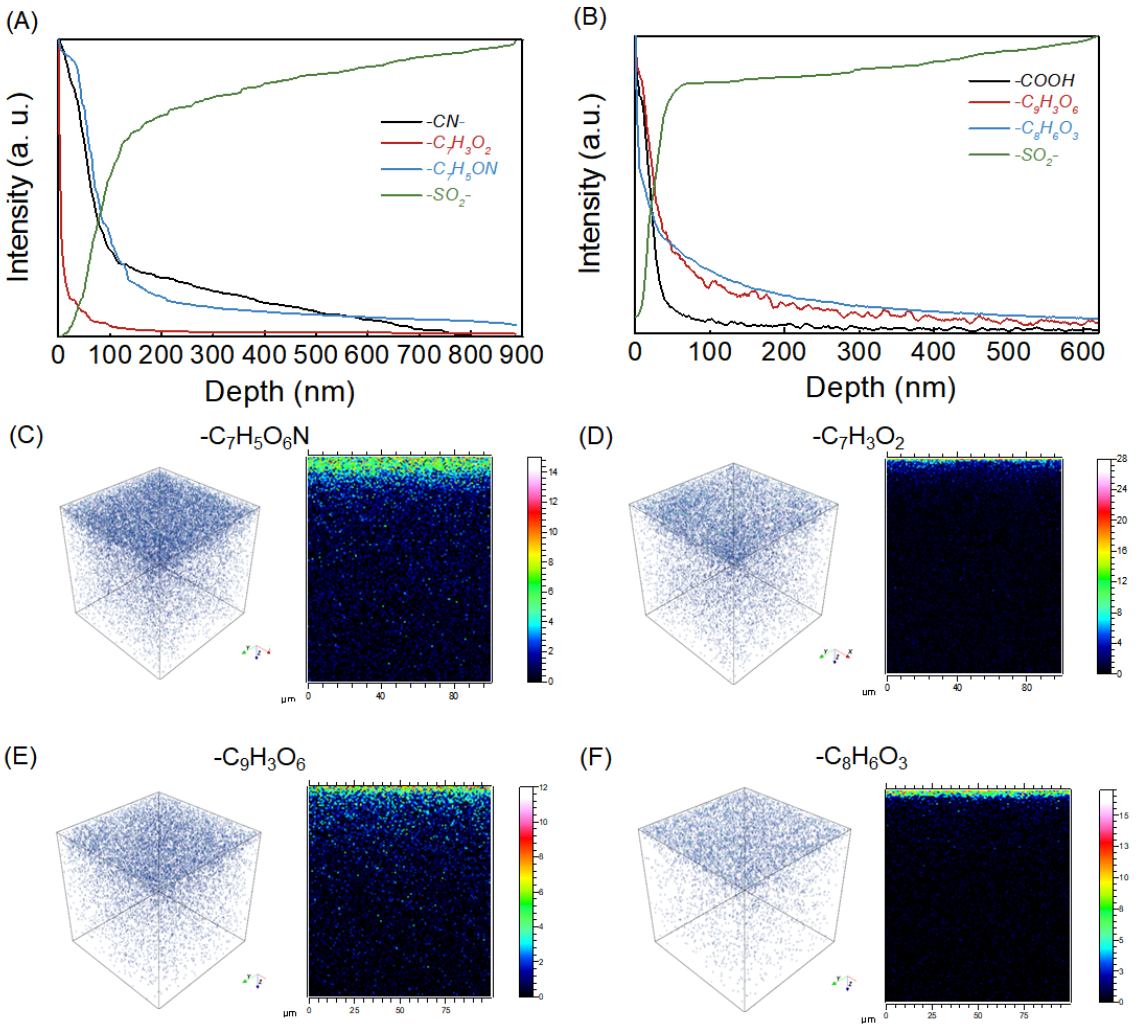

Fig. S27. ToF-SIMS normalized depth profiling of several typical ion fragments on the surface of the (A) SW30 and (B) DHMBA membranes, respectively. (C, D) 3D render and cross-section of two typical fragments in the SW30 membrane . (E, F) 3D render and cross-section of two typical fragments in the DHMBA membrane.

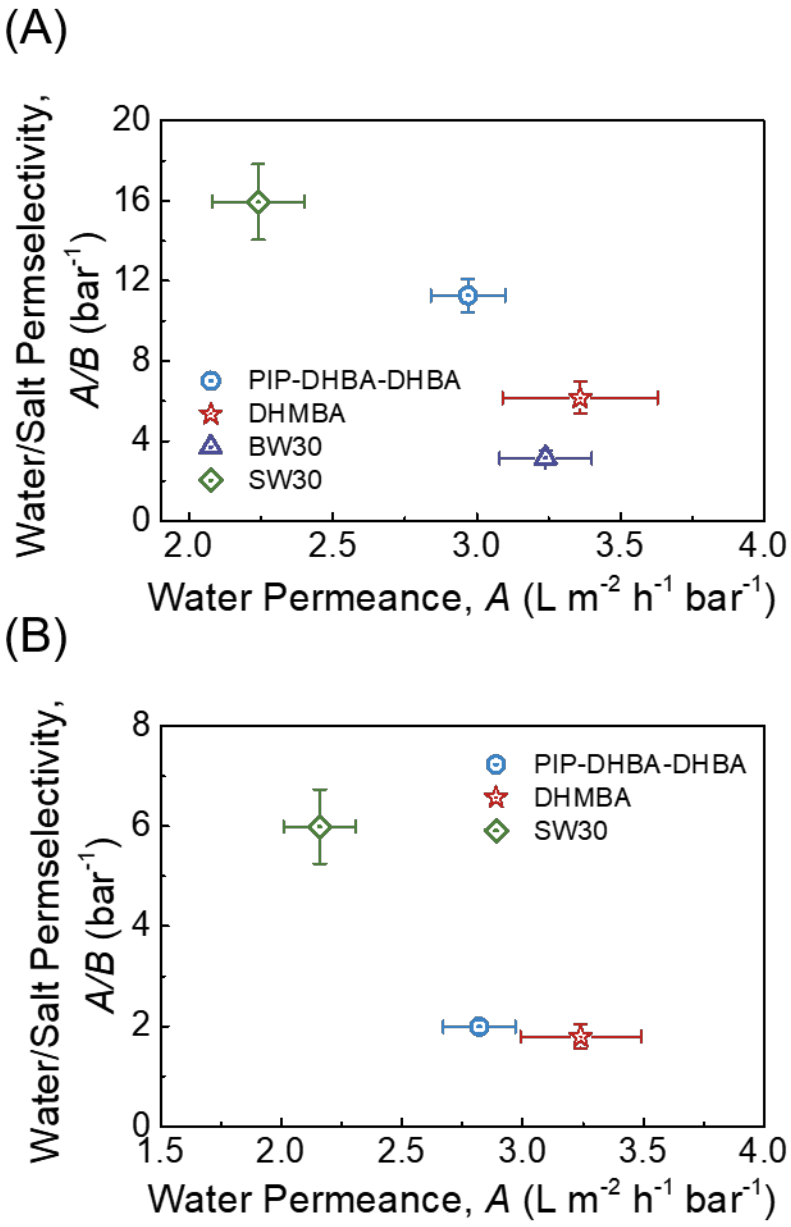

Fig. S28. Permselectivity analysis of the DHMBA, PIP-DHBA-DHBA, BW30, and SW30 membranes toward (A) a 2,000 mg L^{-1} NaCl feed solution and (B) a 35,000 mg L^{-1} NaCl feed solution. The water permeance, *A*, was calculated using pure water. The salt permeability coefficient, *B*, was calculated using equation S5.

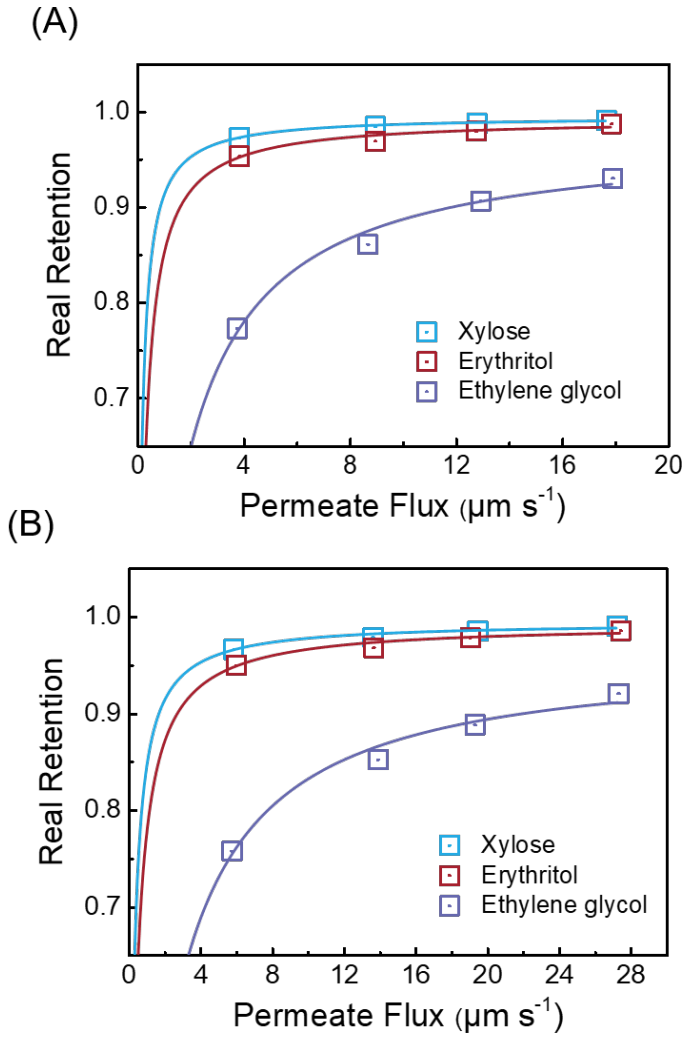

Fig. S29. Dependence of membrane real retention of neutral organic tracers on membrane permeate water flux. Ethylene glycol, erythritol, and xylose were utilized for the measurements with (A) SW30 and (B) DHMBA membranes. Experiments were conducted using a bench-scale crossflow filtration system. In each experiment, a single organic tracer was used at a feed concentration of 50 mg L^{-1} (as TOC). Permeate samples were collected under pressures of 27.6, 20.7, 13.8, and 6.9 bar for both membranes. Fitting is based on the membrane pore hindrance transport mode. In all the experiments, temperature was maintained at 22.0±0.5 °C, and the crossflow velocity was set at 21.4 cm s^{-1}. The estimated effective pore radii of the DHMBA and SW30 membranes, obtained from fitting the solute rejection data to the hydrodynamic pore transport model, are comparable (0.289 and 0.286 nm, respectively).

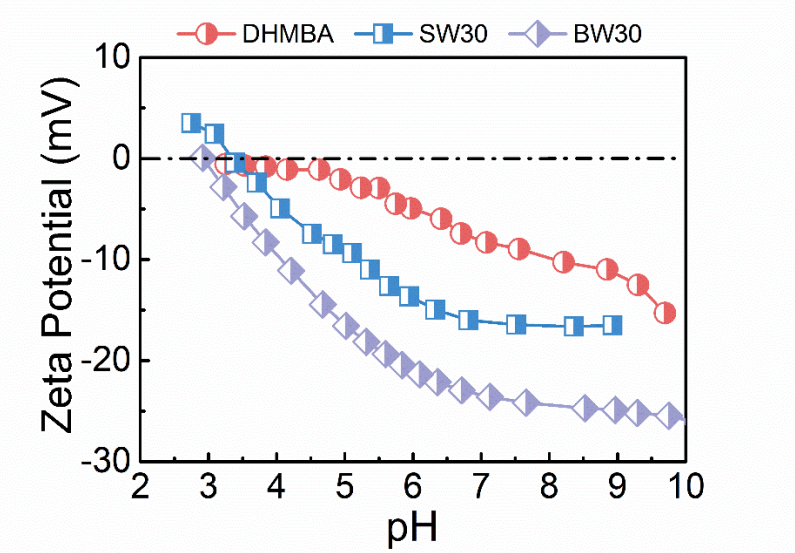

Fig. S30. Zeta potentials of the SW30, BW30, and DHMBA membranes as a function of pH. The surface zeta potential was recorded with a background KCl (1 mM) solution, and the pH was adjusted from 3 to 10 using NaOH (0.1 M) and HCl (0.1 M) solutions.

Related discussion:

The zeta potential of the DHMBA membrane was compared to the commercial SW30 and BW30 membranes (fig. S30). Conventional polyamide RO membranes (BW30 and SW30 membranes) possessed isoelectric points of around pH 3.0–3.5, which points to their typical amphiprotic nature. In comparison, the DHMBA membrane exhibited a weak negative charge over the entire pH range. Note that the number of surface carboxylic acid groups was likely reduced compared to conventional polyamide membranes due to the self-polymerization and crosslinking reaction (with TMC), which may contribute to the decreased surface negative charge.

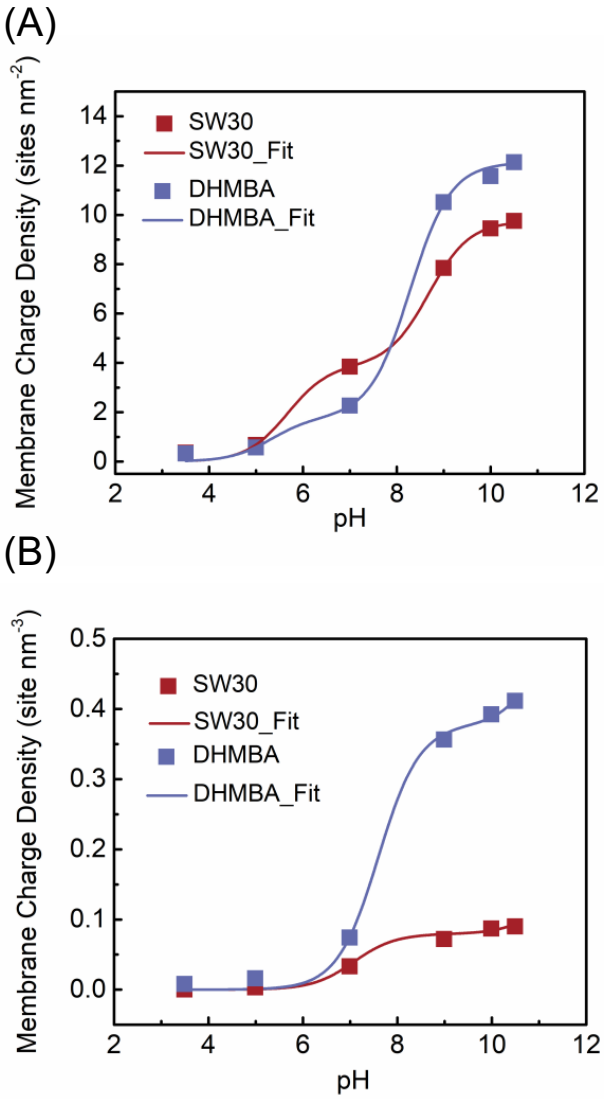

Fig. S31. (A) Areal ionized carboxyl group density, $[\mathrm{R-COO^-}]_{A_m}$, as a function of pH for the SW30 and DHMBA membranes. (B) Volumetric ionized carboxyl group density, $[\mathrm{R-COO^-}]_{V_m}$, representing the thickness-normalized ionized carboxyl group of the membrane, as a function of pH for the SW30 and DHMBA membranes. The fitting curves were based on equation S12.

Relevant discussion:

The areal and volumetric ionized carboxyl group densities were fitted by equation S12, resulting in two $p\mathrm{K_a}$ values. The values of $p\mathrm{K_{a,1}}$ are 5.67 and 5.32 for SW30 and DHMBA membranes, respectively. The values of $p\mathrm{K_{a,2}}$ are 8.68 and 8.28 for SW30 and DHMBA membranes, respectively. Generally, $p\mathrm{K_{a,1}}$ corresponds to carboxyl groups on the membrane surface, while $p\mathrm{K_{a,2}}$ corresponds to carboxyl groups within the membrane (*48*). As shown in fig. S31A, the SW30 membrane exhibits higher areal ionized carboxyl group density than the DHMBA membrane around the $p\mathrm{K_{a,1}}$, indicating that the SW30 membrane possesses more carboxyl groups on the surface. As shown in fig. S31B, the DHMBA membrane exhibits a much higher volumetric carboxyl concentration than the SW30 membrane, demonstrating that the DHMBA membrane has more abundant carboxyl groups within the membrane matrix.

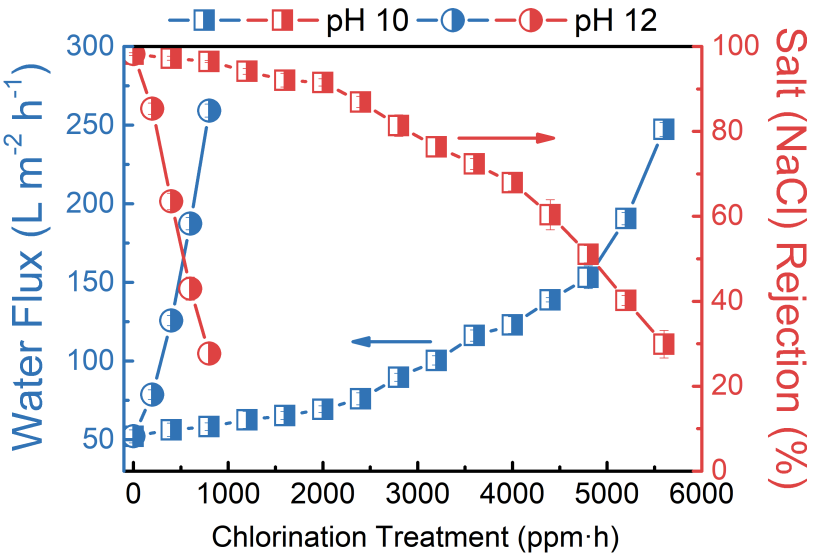

Fig. S32. Separation performance (water flux and salt rejection) of the DHMBA membrane exposed to NaOCl aqueous solution at pH 10 and 12. The DHMBA membrane was immersed in NaOCl solution under continuous stirring at 25 °C, and the solution pH was adjusted using HCl (aq., 1.0 M). The chlorine solution (50 mg L^{-1}) was replaced with a fresh solution every 24 hours. At certain times, membrane sheets were removed from the solution, rinsed thoroughly with DI water, and tested for their desalination performance under the following experimental conditions: an effective membrane area of 15.0 cm^2, 2,000 mg L^{-1} NaCl feed solution, crossflow velocity of 40.0 cm s^{-1}, constant pressure of 15.5 bar, and temperature of at 25±0.5 °C.

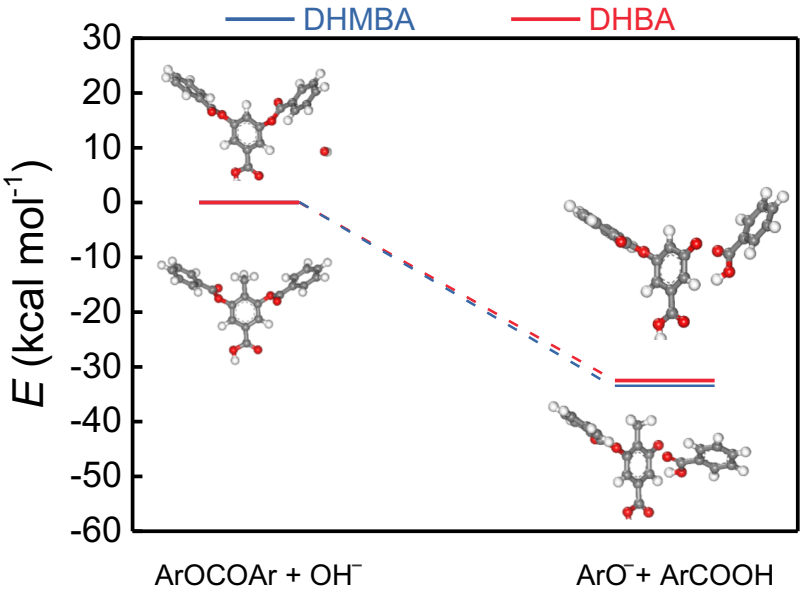

Fig. S33. Energy variation of the ester bond in DHBA and DHMBA-based model compounds toward attack by hydroxyl ions.

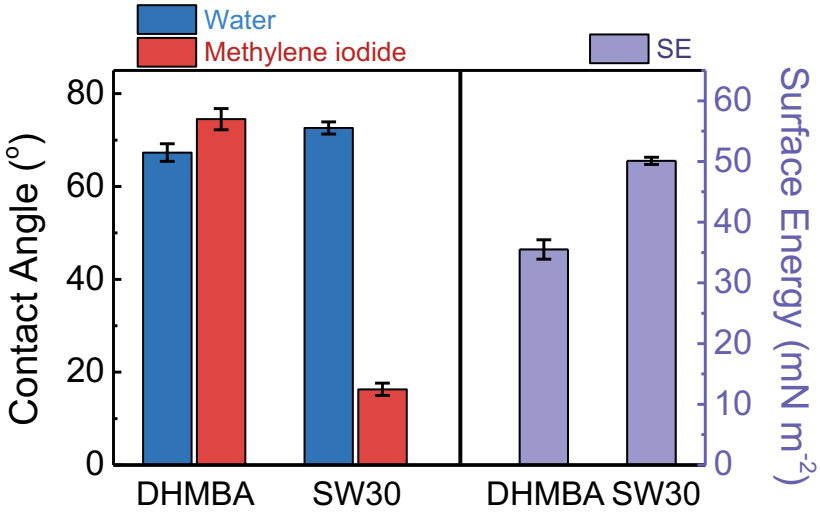

Fig. S34. Contact angles and surface energy (SE) of the DHMBA and SW30 membranes. A drop of DI water or methylene iodide (1 μL) was placed on the surface of membranes with a contact time of 10 seconds. Eight measurements were taken at different locations for each sample. Error bars represent standard deviation. The surface energy components were estimated by the Owens−Wendt method using the experimentally determined intrinsic contact angles of water and methylene iodide (*49*).

Related discussion:

The DHMBA membrane has a lower water contact angle than the SW30 membrane, thus providing a higher barrier for heterogeneous nucleation (fig. S34). Analysis of surface energy components based on water contact angles and methylene iodide contact angles is summarized in table S8. Although the total surface energy of the DHMBA membrane (35.5 mN m^{-1}) is lower than that of the SW30 membrane (50.1 mN m^{-1}), its polar portion (20.8 mN m^{-1}) is much greater than that of the SW30 membrane (5.1 mN m^{-1}). Such higher polarity of the DHMBA membrane allows the establishment of a more significant hydration layer on its surface than the SW30 membrane, which provides a larger barrier to the adhesion of bulk crystals and organic foulants on the surface.

Table S1. The bonding dissociation energy ΔE (eV), energy gap $\Delta E_{\text{L-H}}$ (eV), Mulliken population, and the condensed Fukui functions f_k^- of the DHBA, DHMBA, and MPD repeating units.

Systems	ΔE_{b}	$\Delta E_{\text{L-H}}$	**Mulliken Population** [a]	f_k^- [b]
DHBA	1.99	3.67	C1=-0.097; C2=-0.115; C3=-0.065; C4=0.306; C5=0.522 H1=0.128; H2=0.124; H3=0.123 O1=-0.487; O2=-0.458	C1=0.083; C2=0.030; C3=0.088 H1=0.047; H2=0.038; H3=0.049
DHMBA	2.04	3.81	C1=-0.089; C2=-0.030; C3=-0.078; C4=0.312; C5=0.517 H1=0.126; H2=0.123; O1=-0.497; O2=-0.457	C1=0.085; C3=0.075; H1=0.048; H2=0.048;
MPD	—	3.13	C1=-0.147; C2=-0.068; C3=-0.132; C4=-0.166 H1=0.117; H2=0.095; H3=0.100; H4=0.134	C1=0.098; C2=0.031; C3=0.100; C4=0.037 H1=0.053; H2=0.043; H3=0.058; H4=0.035

[a] Mulliken population of C and H atoms, which are labeled in fig. S12. Positive values represent the loss of electrons while the negative values refer to the gain of electrons, both of which are relative to free atoms;
[b] The condensed Fukui functions f_k^- of electrophilic attack reaction (direct aromatic chlorination). Atom numbers are labeled in fig. S12. A lower f_k^- indicates lower potential of the molecule to be attacked by an electrophile.

Table S2. XPS elemental composition of fabricated polyester membranes.

Membrane	Atomic Concentration (%)			
	C	O	O/C	CD [a] (%)
DHMBA	73.5	26.5	0.36	>92%
PIP-DHBA-DHBA	72.2	27.7	0.38	>88%

[a] CD denotes the cross-linking degree of the polymer network.

Table S3. Thickness measurements obtained by laser ellipsometry of the active layer of the DHMBA and SW30 membranes.

Membrane	Thickness (nm)	MSE [a]
DHMBA	33.93±0.83	3.243×10^{-10}
SW30	105.10±0.62	2.321×10^{-12}

[a] Mean squared error.

Table S4. Chemical composition of simulated and practical (real) seawater (Qingdao City, China, 120.0358°E, 35.8139°N).

Content	Mass Concentration (mg L^{-1})	
	Simulated Seawater [a]	**Practical Seawater**
K^+	/	380
Na^+	10941	10840
Ca^{2+}	432	424
Mg^{2+}	1291	1259
Sr^{2+}	/	4.05
Cl^-	19472	15500
Br^-	/	106
SO_4^{2-}	2707	2249
HCO_3^-	/	96.7
B (boron)	/	4.24
pH	7.7±0.1	8.2±0.1

[a] The simulated seawater contained 27.8 wt% NaCl, 1.2 wt% $CaCl_2$, 5.2 wt% $MgCl_2 \cdot 6H_2O$, and 3.4 wt% $MgSO_4$.

Table S5. Boric concentrations and rejection of the two feed solutions by the DHMBA membrane.

	Boron in Feed Solution (mg L^{-1})	Boron in Permeate Solution (mg L^{-1})	Rejection (%)
Solution 1 [a]	5.1	0.32–0.35	93.2±0.3
Solution 2 [b]	87.4	7.1–7.9	91.2±0.5

[a] Simulated seawater containing 29.0 mg L^{-1} boron acid;
[b] A feed water containing 500.0 mg L^{-1} boron acid.

Table S6. Surface element composition (determined via XPS) of the SW30 and DHMBA membranes after the chlorine-resistance experiments.

Membrane		Atomic Composition (%)		
		C	**O**	**Cl**
pH = 0.0	SW30	67.99	16.52	5.97
	DHMBA	76.28	23.72	< 0.1
pH = 7.0	SW30	69.51	16.58	4.65
	DHMBA	70.28	29.72	< 0.1
pH = 9.0	SW30	71.61	16.00	3.77
	DHMBA	74.18	25.82	< 0.1

[a] For the SW30 membrane, a total CT_{FC} of 8,000 ppm·h (50 ppm NaOCl solution for 160 hours) was applied for the three pH conditions.
[b] For the DHMBA membrane, a total CT_{FC} of 100,000 ppm·h (50 ppm NaOCl solution for 2,000 hours) was applied for the three pH conditions.

Table S7. Surface element composition (determined via XPS) of the SW30 and DHMBA membranes after different scaling tests.

	SW30 (SI=0.51)	**DHMBA (SI=0.51)**	**SW30 (SI=0.52)**	**DHMBA (SI=0.52)**
Element	Atomic Composition (%)			
Na	5.39	2.47	1.57	1.83
Ca	0.86	0.23	2.57	0.78
Cl	10.72	11.37	8.72	4.46
S	83.02	85.93	87.08	92.93

Table S8. The water contact angle (WCA), methylene iodide contact angle (MCA), surface energy, and roughness (R_a) of the DHMBA and SW30 membranes.

Membrane	WCA (°)	MCA (°)	Surface Energy (mN m^{-2})	$\gamma^{dispersion}$	γ^{polar}	R_a (nm)
DHMBA	67.3±1.9	74.5±2.3	35.5±1.6	14.7±1.0	20.8±0.7	2.36±0.32
SW30	72.6±1.3	16.3±1.3	50.1±0.6	45.1±0.1	5.1±0.6	74.90±2.41

Relevant discussion:

The surface energy of the DHMBA and SW30 membranes was estimated by the Owens and Wendt method based on the measured water and methylene iodide contact angles (*50*). $\gamma^{dispersion}$ indicates the surface energy component stemming from dispersion force, whereas γ^{polar} refers to the surface energy arising from hydrogen bonding and dipole-dipole interactions. The larger γ^{polar} for the DHMBA membrane indicates a stronger hydration layer than the SW30 membrane, further enhancing the scaling and organic fouling resistance of the DHMBA membrane.

Table S9. Surface element composition (determined via XPS) of the DHMBA membrane after a short-term desalination test with practical seawater.

Element	Composition (%)
C	68.58
O	19.17
Na	0.75
Ca	<0.01
Cl	1.13
S	10.3

References and Notes

1. J. R. Werber, C. O. Osuji, M. Elimelech, Materials for next-generation desalination and water purification membranes. *Nat. Rev. Mater.* **1**, 16018–16025 (2016). doi:10.1038/natrevmats.2016.18

2. Y. J. Lim, K. Goh, M. Kurihara, R. Wang, Seawater desalination by reverse osmosis: Current development and future challenges in membrane fabrication – A review. *J. Membr. Sci.* **629**, 119292 (2021). doi:10.1016/j.memsci.2021.119292

3. G. M. Geise, Why polyamide reverse-osmosis membranes work so well. *Science* **371**, 31–32 (2021). doi:10.1126/science.abe9741 Medline

4. Z. Wang, S. Liang, Y. Kang, W. Zhao, Y. Xia, J. Yang, H. Wang, X. Zhang, Manipulating interfacial polymerization for polymeric nanofilms of composite separation membranes. *Prog. Polym. Sci.* **122**, 101450 (2021). doi:10.1016/j.progpolymsci.2021.101450

5. R. Verbeke, V. Gómez, I. Vankelecom, Chlorine-resistance of reverse osmosis (RO) polyamide membranes. *Prog. Polym. Sci.* **72**, 1–15 (2017). doi:10.1016/j.progpolymsci.2017.05.003

6. M. Qasim, M. Badrelzaman, N. N. Darwish, N. A. Darwish, N. Hilal, Reverse osmosis desalination: A state-of-the-art review. *Desalination* **459**, 59–104 (2019). doi:10.1016/j.desal.2019.02.008

7. H. B. Park, B. D. Freeman, Z. B. Zhang, M. Sankir, J. E. McGrath, Highly chlorine-tolerant polymers for desalination. *Angew. Chem. Int. Ed.* **47**, 6019–6024 (2008). doi:10.1002/anie.200800454 Medline

8. R. Verbeke, D. M. Davenport, T. Stassin, S. Eyley, M. Dickmann, A. J. Cruz, P. Dara, C. L. Ritt, C. Bogaerts, W. Egger, R. Ameloot, J. Meersschaut, W. Thielemans, G. Koeckelberghs, M. Elimelech, I. Vankelecom, Chlorine-resistant epoxide-based membranes for sustainable water desalination. *Environ. Sci. Technol. Lett.* **8**, 818–824 (2021). doi:10.1021/acs.estlett.1c00515

9. Y. Yao, P. Zhang, C. Jiang, R. DuChanois, X. Zhang, M. Elimelech, High performance polyester reverse osmosis desalination membrane with chlorine resistance. *Nat. Sustain.* **4**, 138–146 (2021). doi:10.1038/s41893-020-00619-w

10. G. Tchobanoglous, H. D. Stensel, R. Tsuchihashi, F. L. Burton, *Wastewater Engineering: Treatment and Resource Recovery* (McGraw-Hill, ed. 5, 2013).

11. E. Pop, M. Huang, M. E. Brewster, N. Bodor, A theoretical study of the hydrolysis of some sterically hindered phenolic esters. *Int. J. Quantum Chem.* **44** (S19), 77–85 (1992). doi:10.1002/qua.560440711

12. X. Ma, Z. Yao, Z. Yang, H. Guo, Z. Xu, C. Y. Tang, M. Elimelech. Nanofoaming of polyamide desalination membranes to tune permeability and selectivity. *Environ. Sci. Technol.* **5**, 123–130 (2018).

13. M. F. Jimenez-Solomon, Q. Song, K. E. Jelfs, M. Munoz-Ibanez, A. G. Livingston, Polymer nanofilms with enhanced microporosity by interfacial polymerization. *Nat. Mater.* **15**, 760–767 (2016). doi:10.1038/nmat4638 Medline

14. S. J. Vanhook, M. F. Schatz, J. Swift, W. McCormick, H. L. Swinney, Long-wavelength surface-tension-driven Bénard convection: Experiment and theory. *J. Fluid Mech.* **345**, 45–78 (1997). doi:10.1017/S0022112097006101

15. D. Ren, Y. T. Jin, T. Y. Liu, X. Wang, Phenanthroline-based polyarylate porous membranes with rapid water transport for metal cation separation. *ACS Appl. Mater. Interfaces* **12**, 7605–7616 (2020). doi:10.1021/acsami.9b22086 Medline

16. R. Bernstein, S. Belfer, V. Freger, Toward improved boron removal in RO by membrane modification: Feasibility and challenges. *Environ. Sci. Technol.* **45**, 3613–3620 (2011). doi:10.1021/es103991u Medline

17. K. L. Tu, L. D. Nghiem, A. R. Chivas, Boron removal by reverse osmosis membranes in seawater desalination applications. *Separ. Purif. Tech.* **75**, 87–101 (2010). doi:10.1016/j.seppur.2010.07.021

18. A. Tal, Seeking sustainability: Israel's evolving water management strategy. *Science* **313**, 1081–1084 (2006). doi:10.1126/science.1126011 Medline

19. A. Antony, R. Fudianto, S. Cox, G. Leslie, Assessing the oxidative degradation of polyamide reverse osmosis membrane-accelerated ageing with hypochlorite exposure. *J. Membr. Sci.* **347**, 159–164 (2010). doi:10.1016/j.memsci.2009.10.018

20. K. Huang, K. P. Reber, M. D. Toomey, H. Haflich, J. A. Howarter, A. D. Shah, Reactivity of the polyamide membrane monomer with free chlorine: Reaction kinetics, mechanisms, and the role of chloride. *Environ. Sci. Technol.* **53**, 8167–8176 (2019). doi:10.1021/acs.est.9b01446 Medline

21. V. T. Do, C. Y. Tang, M. Reinhard, J. O. Leckie, Degradation of polyamide nanofiltration and reverse osmosis membranes by hypochlorite. *Environ. Sci. Technol.* **46**, 852–859 (2012). doi:10.1021/es203090y Medline

22. B. Delley, An all-electron numerical method for solving the local density functional for polyatomic molecules. *J. Chem. Phys.* **92**, 508–517 (1990). doi:10.1063/1.458452

23. B. Delley, From molecules to solids with the DMol3 approach. *J. Chem. Phys.* **113**, 7756–7764 (2000). doi:10.1063/1.1316015

24. A. D. Becke, A multicenter numerical integration scheme for polyatomic molecules. *J. Chem. Phys.* **88**, 2547–2553 (1988). doi:10.1063/1.454033

25. C. Lee, W. Yang, R. G. Parr, Development of the Colle-Salvetti correlation-energy formula into a functional of the electron density. *Phys. Rev. B Condens. Matter* **37**, 785–789 (1988). doi:10.1103/PhysRevB.37.785 Medline

26. A. Klamt, G. Schüürmann, COSMO: A new approach to dielectric screening in solvents with explicit expressions for the screening energy and its gradient. *J. Chem. Soc.* **5**, 799–805 (1993).

27. B. Delley, The conductor-like screening model for polymers and surfaces. *Mol. Simul.* **32**, 117–123 (2006). doi:10.1080/08927020600589684

28. M. J. Frisch, G. W. Trucks, H. B. Schlegel, G. E. Scuseria, M. A. Robb, J. R. Cheeseman, G. Scalmani, V. Barone, G. A. Petersson, H. Nakatsuji, X. Li, M. Caricato, A. V. Marenich, J. Bloino, B. G. Janesko, R. Gomperts, B. Mennucci, H. P. Hratchian, J. V. Ortiz, A. F. Izmaylov, J. L. Sonnenberg, D. Williams-Young, F. Ding, F. Lipparini, F. Egidi, J. Goings, B. Peng, A. Petrone, T. Henderson, D. Ranasinghe, V. G. Zakrzewski, J. Gao, N. Rega, G. Zheng, W. Liang, M. Hada, M. Ehara, K. Toyota, R. Fukuda, J. Hasegawa, M. Ishida, T. Nakajima, Y. Honda, O. Kitao, H. Nakai, T. Vreven, K. Throssell, J. A. Montgomery Jr., J. E. Peralta, F. Ogliaro, M. J. Bearpark, J. J. Heyd, E. N. Brothers, K. N. Kudin, V. N. Staroverov, T. A. Keith, R. Kobayashi, J. Normand, K. Raghavachari, A. P. Rendell, J. C. Burant, S. S.

Iyengar, J. Tomasi, M. Cossi, J. M. Millam, M. Klene, C. Adamo, R. Cammi, J. W. Ochterski, R. L. Martin, K. Morokuma, O. Farkas, J. B. Foresman, D. J. Fox, “Gaussian 16, revision A.03” (Gaussian, 2016).

29. R. G. Parr, W. Yang, *Density-Functional Theory of Atoms and Molecules* (Oxford Univ. Press, 1989).

30. Y. Yao, W. Zhang, Y. Du, M. Li, L. Wang, X. Zhang, Toward enhancing the chlorine resistance of reverse osmosis membranes: An effective strategy via an end-capping technology. *Environ. Sci. Technol.* **53**, 1296–1304 (2019). doi:10.1021/acs.est.8b06006 Medline

31. C. L. Ritt, T. Stassin, D. M. Davenport, R. M. DuChanois, I. Nulens, Z. Yang, A. Ben-Zvi, N. Segev-Mark, M. Elimelech, C. Y. Tang, G. Z. Ramon, I. F. J. Vankelecom, R. Verbeke, The Open Membrane Database: Synthesis-structure-performance relationships of reverse osmosis membranes. *J. Membr. Sci.* **641**, 119927 (2022). doi:10.1016/j.memsci.2021.119927

32. K. Zuo, X. Zhang, X. Huang, E. F. Oliveira, H. Guo, T. Zhai, W. Wang, P. J. J. Alvarez, M. Elimelech, P. M. Ajayan, J. Lou, Q. Li, Ultrahigh resistance of hexagonal boron nitride to mineral scale formation. *Nat. Commun.* **13**, 4523 (2022). doi:10.1038/s41467-022-32193-4 Medline

33. T. Cao, J. Rolf, Z. Wang, C. Violet, M. Elimelech, Distinct impacts of natural organic matter and colloidal particles on gypsum crystallization. *Water Res.* **218**, 118500 (2022). doi:10.1016/j.watres.2022.118500 Medline

34. A. H. Truesdell, B. F. Jones, WATEQ, a computer program for calculating chemical equilibria of natural waters. *J. Res. U.S. Geol. Surv.* **2**, 233–248 (1974).

35. S. Tang, Y. Ji, K. Ge, Crystallization kinetics and mechanisms of calcium sulfate dihydrate: Experimental investigation and theoretical analysis. *Ind. Eng. Chem. Res.* **59**, 21676–21684 (2020). doi:10.1021/acs.iecr.0c04220

36. S. Lee, M. Elimelech, Relating organic fouling of reverse osmosis membranes to intermolecular adhesion forces. *Environ. Sci. Technol.* **40**, 980–987 (2006). doi:10.1021/es051825h Medline

37. D. Chen, J. R. Werber, X. Zhao, M. Elimelech, A facile method to quantify the carboxyl group areal density in the active layer of polyamide thin-film composite membranes. *J. Membr. Sci.* **534**, 100–108 (2017). doi:10.1016/j.memsci.2017.04.001

38. O. Coronell, B. J. Mariñas, X. Zhang, D. G. Cahill, Quantification of functional groups and modeling of their ionization behavior in the active layer of FT30 reverse osmosis membrane. *Environ. Sci. Technol.* **42**, 5260–5266 (2008). doi:10.1021/es8002712 Medline

39. L. D. Nghiem, A. I. Schäfer, M. Elimelech, Removal of natural hormones by nanofiltration membranes: Measurement, modeling, and mechanisms. *Environ. Sci. Technol.* **38**, 1888–1896 (2004). doi:10.1021/es034952r Medline

40. D. R. Lide, *Handbook of Chemistry and Physics* (CRC Press, 2010).

41. D. N. Rocha, A. P. Rosa, A. C. Borges, J. H. H. Falconi, L. Covell, M. A. Martins, Impacts of organic solvent toxicity on resource recovery from Scenedesmus obliquus biomass after lipid extraction. *Biomass Bioenergy* **177**, 106948 (2023). doi:10.1016/j.biombioe.2023.106948

42. J. Rolf, T. Cao, X. Huang, C. Boo, Q. Li, M. Elimelech, Inorganic scaling in membrane desalination: Models, mechanisms, and characterization methods. *Environ. Sci. Technol.* **56**, 7484–7511 (2022). doi:10.1021/acs.est.2c01858 Medline

43. C. Y. Tang, T. H. Chong, A. G. Fane, Colloidal interactions and fouling of NF and RO membranes: A review. *Adv. Colloid Interface Sci.* **164**, 126–143 (2011). doi:10.1016/j.cis.2010.10.007 Medline

44. Y. Mo, A. Tiraferri, N. Y. Yip, A. Adout, X. Huang, M. Elimelech, Improved antifouling properties of polyamide nanofiltration membranes by reducing the density of surface carboxyl groups. *Environ. Sci. Technol.* **46**, 13253–13261 (2012). doi:10.1021/es303673p Medline

45. Q. Wang, W. Lin, S. Chou, P. Dai, X. Huang, Patterned membranes for improving hydrodynamic properties and mitigating membrane fouling in water treatment: A review. *Water Res.* **236**, 119943 (2023). doi:10.1016/j.watres.2023.119943 Medline

46. X. Song, B. Gan, S. Qi, H. Guo, C. Y. Tang, Y. Zhou, C. Gao, Intrinsic nanoscale structure of thin film composite polyamide membranes: Connectivity, defects, and structure–property correlation. *Environ. Sci. Technol.* **54**, 3559–3569 (2020). doi:10.1021/acs.est.9b05892 Medline

47. C. Lu, C. Hu, C. L. Ritt, X. Hua, J. Sun, H. Xia, Y. Liu, D. W. Li, B. Ma, M. Elimelech, J. Qu, In situ characterization of dehydration during ion transport in polymeric nanochannels. *J. Am. Chem. Soc.* **143**, 14242–14252 (2021). doi:10.1021/jacs.1c05765 Medline

48. C. L. Ritt, J. R. Werber, M. Wang, Z. Yang, Y. Zhao, H. J. Kulik, M. Elimelech, Ionization behavior of nanoporous polyamide membranes. *Proc. Natl. Acad. Sci. U.S.A.* **117**, 30191–30200 (2020). doi:10.1073/pnas.2008421117 Medline

49. C. Boo, J. Lee, M. Elimelech, Engineering surface energy and nanostructure of microporous films for expanded membrane distillation applications. *Environ. Sci. Technol.* **50**, 8112–8119 (2016). doi:10.1021/acs.est.6b02316 Medline

50. D. K. Owens, R. C. Wendt, Estimation of the surface free energy of polymers. *J. Appl. Polym. Sci.* **13**, 1741–1747 (1969). doi:10.1002/app.1969.070130815